ACS SENSORS
Open Access

pubs.acs.org/acssensors
Article

Biodegradable Smart Face Mask for Cough Acoustic Sensing

Mohammad Javad Bathaei, Ata Golparvar, Sina Hashemi Zadeh, Denys Nikolayev, Filipe Arroyo Cardoso, and Clementine M. Boutry*

Cite This: https://doi.org/10.1021/acssensors.5c04572
Read Online

ACCESS | Metrics & More | Article Recommendations | Supporting Information

ABSTRACT: We introduce Green Cough Sense, a biodegradable, battery-free smart face mask that incorporates a flexible, passive microphone for sensing cough acoustics in pulmonology. The device integrates a mesoscale-patterned 3 by 3 array of 1 cm^2 circular drum-like membranes with a patch antenna, a planar resonator comprising a metallic radiating patch over a grounded dielectric substrate. Cough-induced acoustic vibrations are transduced into measurable shifts in the electromagnetic reflection coefficient ($|S_{11}|$), which are measured by a vector network analyzer operating in zero-span mode for high-fidelity characterization. The system is fabricated entirely from sustainably sourced, biodegradable materials, including cellulose acetate, poly(lactic acid), and zinc, via a new green manufacturing process that combines laser machining with solvent- and adhesive-free low-temperature lamination technique with maximum bonding strength reaching 5.8 N/mm. Experimental validation of the mechanoacoustic response demonstrates absolute sensitivity of 0.045 µm/Hz; *in vitro* characterizations under monotone excitation show sensitivity of 0.13%/Pa; *in situ* validation with human participants confirms detection of mild, moderate, and severe cough events. Biodegradation under industrial composting confirms material breakdown with over 90% weight loss after 100 days, supporting a zero-waste end-of-life strategy.

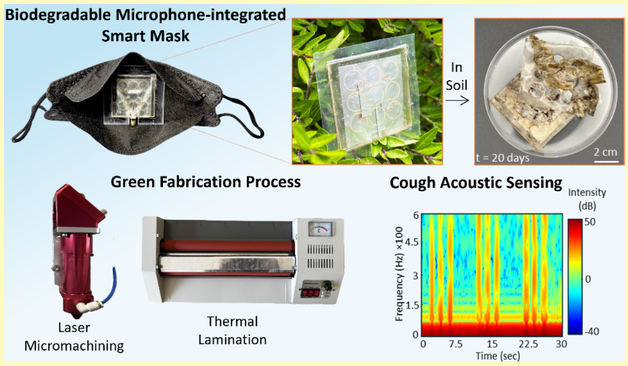

KEYWORDS: *biodegradable devices, cough acoustics, green fabrication, planar resonator, smart mask*

Cough is a key early sign of respiratory disease, signaling a range of conditions from the common cold to serious chronic infections like tuberculosis and chronic obstructive pulmonary disease (COPD).[1,2] Acoustic cough signatures—such as frequency, intensity, duration, and spectral features—may offer valuable diagnostic and prognostic insights, serving as early indicators of respiratory distress and enabling close monitoring of disease progression before severe clinical symptoms emerge.[3−5] For instance, persistent or atypical cough patterns have long been utilized in clinical assessments, particularly in monitoring the spread of infectious respiratory pathogens.[6−8] However, Conventional diagnostic methods such as radiological imaging, sputum microscopy, and lab-based molecular tests are slow, resource-intensive, and reliant on specialized personnel and infrastructure.[9−11] They require invasive sample collection and repeated clinic visits, which can be logistically challenging, and especially difficult for individuals already struggling with respiratory symptoms and reported to be increasing the risk of disease transmission within healthcare settings.[12]

Advances in wearables have enabled non-invasive, continuous monitoring of respiratory health indicators, including chemical, physiological, and acoustic signals.[13,14] Chemical metabolite detection in breath (e.g., volatile organic compounds (VOCs), inorganic gases, pathogens) may find increasing use in early diagnostics of diseases like COPD.[15] However, VOCs show cross-sensitivity with ambient pollutants, diet, medications, and endogenous metabolites (e.g., specificity dropped to 55% in smokers).[16−18] Physiological markers such as breathing rate and tidal volume (typical normal values: 12−20 breaths per minute or <500 mL) are utilized to assess respiratory function, yet their diagnostic specificity is limited, as their values can be altered by non-respiratory factors such as physical activity, anxiety, and fever.[19,20]

Cough acoustics monitoring is event-based, analyzing discrete coughs rather than relying on continuous breath sampling.[21] Distinct acoustic signatures have been identified for respiratory diseases such as COPD, asthma, and tuberculosis, with reported specificities above 85%.[4,22,23] This is because cough acoustics are minimally influenced by ambient metabolites, dietary compounds, or physical exertion.[24] By analyzing key acoustic features such as frequency components, amplitude,

Received: December 1, 2025
Revised: April 21, 2026
Accepted: May 6, 2026

and duration, AI-assisted systems objectively track cough occurrence and patterns in real time, providing disease progression monitoring.[25,26] To date, all demonstrations of cough monitoring have relied on active discrete/built-in microphones or on dedicated microphones installed in patient rooms or clinical facilities.[27,28] However, these setups rely on wired connections and fixed power sources, requiring patients to remain within microphone range, and pose challenges for continuous, real-time monitoring due to user compliance with device placement.[27−29]

Embedding acoustic sensors into face masks offers a discreet way to monitor coughs in real time, turning a preventive tool into a smart diagnostic device. However, these mask-based systems typically operate wirelessly either through integrated Bluetooth modules or by connecting a patch antenna to an active sensor or load circuit.[14,30] In both cases, they rely on active microphones, battery-powered electronics, and non-biodegradable components, which are bulky and require periodic battery replacement. In addition, when discarded after single use, these systems contribute to electronic waste and introduce additional environmental risks, including microplastic contamination, marine pollution, and toxic emissions from incineration.[14,30,31] Unsustainable materials and conventional fabrication methods are the root cause of this issue, generating hazardous waste during production and hindering environmentally friendly disposal at the end of life. In 2022, global electronic waste reached 62 million metric tons, with an annual increase of 2.6 million tons.[32] This growth is largely driven by the rapid turnover of short-lifecycle electronic devices that lack viable end-of-life strategies.[32] These limitations pose a significant barrier to the scalable deployment of smart face masks and underscore the urgent need for sustainable alternatives in both material selection and system integration.

Developing a sustainable cough monitoring system for large-scale use requires sustainable materials and green fabrication processes that enable cost-effective and scalable production. Biodegradable films such as poly (lactic acid) (PLA) and cellulose acetate (CA) have conventionally been produced from petroleum-based precursors through energy-intensive synthesis methods (e.g., polycondensation, ring-opening polymerization, and acetylation) and processed using organic solvents like chloroform, acetone, and dichloromethane, which pose serious environmental and health hazards during handling and disposal.[33,34] Recent advances use renewable raw precursors such as fermented corn starch and wood pulp to produce biodegradable granules that can be processed via roll-to-roll melt extrusion for film fabrication and are now commercially available for PLA and CA.[35−39] To date, these green-produced granules have primarily been solubilized with organic solvents for fabricating biodegradable layers via solution casting, spin coating, or for formulating inks in 3D printing and spray coating processes.[40−42] In addition, patterning of these films often relies on photolithography, which generates toxic chemical waste, or metallization via physical vapor deposition (PVD), a process with high energy consumption.[42,43] These practices compromise the overall sustainability of the process, ultimately making it non-green.

Solvent-free roll-to-roll offers a scalable and green approach to multilayer flexible electronics fabrication. Within this context, laser patterning and lamination have become key technologies in printed electronics.[44] Laser processing offers high-resolution, mask-free patterning with minimal material loss, while lamination enables continuous, solvent-free, and low-temperature integration of multilayer structures.[33,45,46] These techniques eliminate the need for photolithography and chemical etchants, making them well aligned with principles of sustainable manufacturing.[42] Although extensively applied to conventional substrates such as polyethylene terephthalate (PET), polyimide (PI), and polyethylene naphthalate (PEN),[47] extending these fabrication methods for integration of green-produced films could present a promising route toward fully biodegradable and sustainably produced electronic devices.

To meet the growing demand for scalable, eco-friendly cough monitoring technologies, we introduce Green Cough Sense: a biodegradable passive microphone integrated into a single-use face mask. Unlike traditional non-biodegradable, battery-powered smart face masks, our device enables acoustic sensing via a membrane-integrated patch antenna whose electromagnetic reflection coefficient is modulated by sound-induced membrane vibrations. These devices are fabricated entirely from sustainably sourced materials using a green fabrication process introduced in this work, by combining laser processing and thermal lamination, enabling the manufacturing of biodegradable devices at scale.

■ EXPERIMENTAL SECTION

Materials

Zinc (10 μm, 99.9%, ZN00-FL-000260, Goodfellow, Germany), poly(-lactic acid) (PLA, 50 μm and 100 μm, ME34-FM-000100, Goodfellow, Germany), and cellulose acetate (CA, 25 μm, 100 μm, and 500 μm, AC31-FM-000300, Goodfellow, Germany) foils were all sourced commercially. PLA and CA are produced via green manufacturing processes from renewable biomass sources such as corn starch and wood pulp byproducts,[36,37] while zinc is sustainably sourced and 85%-recyclable.[48] All foils were obtained pre-rolled and used without further surface modification.

Dielectric Spectroscopy

Dielectric characterization of CA and PLA thin films was carried out using a broadband open-ended coaxial probe (DAK1.2E-TL) connected to a vector network analyzer (VNA). The films were all sourced from a commercial supplier as mentioned earlier (Goodfellow, Germany) with thicknesses below the free-space wavelength (λ_0) ($\lambda_0/10$) to ensure compatibility with the thin-layer measurement assumptions. The VNA was calibrated using standard short, open, and load measurements to correct for probe and cable mismatch. To address air-gap-induced errors between the probe and sample, an effective air-gap calibration was performed following the proposed method.[49] This was done by measuring several reference materials with well-known permittivity values and comparing the measured reflection data to simulated results. By adjusting the air-gap thickness in the simulation, the value that best matched all measurements was identified. The solver applied a full-wave electromagnetic model based on the method of moments.[49] This effective air-gap value was then used to correct future measurements and improve accuracy.

Square samples were characterized by placing them flat on both sides under the coaxial probe connected to VNA, and data were collected at five discrete points: the center and four points near the periphery. This spatial sampling helped assess in-plane uniformity and reduce local variation effects. To suppress resonance artifacts due to flange truncation, all measurements were conducted with samples placed on a lossy carbon-loaded plastic platform. This setup minimized unwanted reflections and improved measurement stability across the frequency range. Final permittivity values were extracted from the reflection coefficient ($|S_{11}|$), smoothed to reduce noise, and averaged over repeated measurements to ensure accuracy and reproducibility.

https://doi.org/10.1021/acssensors.5c04572
ACS Sens. XXXX, XXX, XXX−XXX

FEM Simulations and Device Design

The patch antenna-based device was modeled and optimized for near 50-ohm impedance matching using CST Microwave Studio. The simulation was based on a multilayer structure, with each layer defined according to material properties and thicknesses provided in the datasheets. From bottom to top, the device consisted of the following layers: a lamination layer (PLA, 50 μm), ground patch (Zinc, 10 μm), substrate (CA, 500 μm), top lamination layer (PLA, 50 μm), spacers (PLA, 100 μm), acoustic resonator (CA, 100 μm), and membrane (CA, 25 μm). A custom materials library for simulation was developed using the measured dielectric properties in this work. To ensure the device could be integrated within a standard face mask, its overall size was limited to 6 to 6 cm. Within this constraint, all dimensions were optimized for performance. A parametric study was conducted using the frequency-domain solver, and S-parameters were monitored to evaluate impedance matching across different configurations. Near-optimal 50-ohm matching was achieved with the following final dimensions (all in cm): lamination layers (W: 6.0, L: 6.2), substrate (W: 5.0, L: 5.0), radiating patch (W: 1.9, L: 2.2), ground patch (W: 3.0, L: 4.0), feed microstrip (W: 0.2, L: 1.8), spacers (W: 1.0, L: 5.0), resonator substrate (W: 5.0, L: 5.0), and membrane (W: 5.0, L: 5.0).

To balance the size constraints of the patch antenna with the need for maximum acoustic sensitivity, a membrane (drum) diameter of 1 cm was selected. This dimension allowed for a sufficiently large displacement under sound pressure, while also enabling the potential integration of multiple drums in an array to enhance the overall effect on antenna performance. The mechanical response of the membrane to sound was simulated using COMSOL Multiphysics. A single drum was modeled based on the membrane material (CA, 25 μm thick; Young's modulus: 1 GPa; density: 1.3 g/cm^3), with density, Young's modulus, and density assigned according to datasheet specifications. To replicate realistic conditions, a layer of air was defined beneath the membrane, incorporating air damping and resistance effects during membrane movement. The membrane diameter was defined parametrically to study its influence on vibrational modes and displacement magnitude. The entire periphery of the membrane was fixed, and a uniform pressure of 1 Pa was applied across the drum surface. The frequency-domain solver was used to simulate membrane displacement, with the applied sound pressure swept from 100 Hz to 800 Hz. The resulting displacement at the center of the membrane was recorded and analyzed.

Laser Micropatterning

A CO_2 laser system (R400, Trotec, Austria) was used to pattern biodegradable foils. Films were affixed to a polished aluminum substrate using Kapton tape to ensure flatness and prevent displacement during processing. For thin films such as zinc and the membrane layer, isopropanol (IPA) was applied between the film and the aluminum substrate to enhance adhesion via van der Waals forces, reduce surface tension, and eliminate wrinkles or bulges that could compromise patterning precision. The excess IPA was removed using a flattened tool typically used for screen printing. Laser parameters—including power, scanning speed, and number of passes—were empirically optimized through trial-and-error to achieve clean edge profiles and avoid thermal damage across different material types and thicknesses. Other available parameters, such as Pulses Per Inch (PPI)/Dots Per Inch (DPI) (600 ppi), Z-offset (0 mm), and pulse frequency (3 kHz), were left at their default factory settings and not adjusted during fabrication. The laser operated in vector cutting mode with air assist enabled to minimize charring and debris. Approximately 3 min are required to cut all layers in a single run. The optimized parameters for the materials used in the device are provided in Table S1 (Supporting Information).

Structural Assembly

3D multilayer stacking of the device was achieved through a solvent-free, low-temperature heated roller lamination process using a low-cost unit (320A, VEVOR, China). To prevent unintended adhesion, Teflon sheets (Grafix Plastics, USA) were placed above and below the films during lamination at 150 °C. The acoustic resonator was constructed by laminating a 25 μm CA membrane onto a 100 μm CA substrate. The patterned zinc ground plane, 500 μm CA antenna substrate, and 50 μm PLA lamination patch were carefully aligned manually using laser-defined registration marks and laminated at 120 °C. Finally, the acoustic resonator was mounted above the patch antenna using 100 μm PLA spacers and laminated at 120 °C with the same process. More than 30 devices were fabricated and tested, achieving a 100% yield with no defects. The lamination process described here was performed manually, taking approximately 10 min to align the layers and assemble three devices per batch. The limited number of devices processed per step, imperfect layer alignments or interlayer sliding during the lamination process (less than 500 μm error), and extended assembly time are attributable to the use of manual, low-cost equipment. In contrast, industrial-scale, fully automated lamination systems with auto-alignment cues, commonly employed in roll-to-roll flexible electronics manufacturing, can significantly increase throughput and enable rapid upscaling with minimal processing time.[50]

Assessment of Lamination Quality

The thickness of laminated film assemblies was evaluated to assess dimensional changes resulting from thermal bonding. Measurements were conducted on three combinations of materials: CA on CA, CA on PLA, and PLA on PLA. A high-precision digital length gauge (Heidenhain-Metro MT 1281, resolution: 0.2 μm) was used to measure the individual film layers before lamination and the bonded assemblies afterward. To evaluate the mechanical integrity and interfacial adhesion of the laminated films, tensile testing was performed in accordance with ASTM D638. Test specimens were prepared in a dog-bone geometry, laser-cut to dimensions suitable for thin polymeric materials. Mechanical testing was carried out using a Dynamic Mechanical Analysis (DMA) system (Q800, TA Instruments, USA). Each specimen was mounted in the grip of the system and subjected to a preload of 0.1 N. Testing was performed under displacement control until either delamination or tensile failure occurred. Force−displacement data were collected and analyzed to quantify tensile strength and the bonding performance between layers.

Membrane Displacement Characterization

Out-of-plane displacement of the cellulosic membrane was characterized using a custom-built measurement setup. A high-precision confocal chromatic displacement sensor (confocalDT IFS 2410, Micro-Epsilon, Germany) was employed to capture membrane deflection with sub-micron resolution. The test structure consisted of a single drum-type resonator with 1 cm diameter, fabricated by laminating a 25 μm-thick CA membrane onto a 100 μm-thick CA substrate. To ensure consistent and accurate measurements, the center of the membrane, corresponding to the focal point of the sensor, was visually marked with a black dot. The laminated assembly was mounted onto a laser-cut polymethyl methacrylate (PMMA) (Plexiglas, The Netherlands) stand using double-sided adhesive tape. A central groove in the stand allowed for unobstructed acoustic wave propagation to the membrane. The confocal sensor was mounted on a separate adjustable fixture and aligned coaxially with the marked center of the membrane to enable precise and repeatable displacement measurements. To minimize external acoustic interference and internal reflections, a custom-designed anechoic chamber was fabricated. The enclosure was constructed from PMMA and internally lined with acoustic absorbent mats (SA-P80, T.akustik, Germany), then fully sealed to dampen ambient noise. Feedthrough ports were integrated into the chamber walls to allow the speaker and confocal sensor to be placed inside while keeping all control electronics, signal generation, and data acquisition systems outside the enclosure.

The membrane was actuated using a 12 V speaker (CDSM-4627-104, Same Sky, USA), driven by a dual H-bridge power amplifier circuit

https://doi.org/10.1021/acssensors.5c04572
ACS Sens. XXXX, XXX, XXX−XXX

based on the L298 driver (STMicroelectronics, Switzerland). As the experiment required only on/off tonal excitation rather than high-fidelity audio playback, this simple setup was sufficient for generating consistent actuation signals without the need for dedicated audio amplifiers. The speaker input was modulated using a signal generator (33210A, Keysight, USA) to sweep the excitation frequency from 400 to 600 Hz. To ensure uniform actuation conditions, a reference microphone (HLWIP02-2, Huacam, China) was positioned near the DUT and used to calibrate the sound pressure level to 90 dB SPL (1 Pa). The audio signal recorded by the reference microphone was analyzed with Audacity software to verify that the output frequency matched the signal generator settings.

Device Resonance Behavior Characterization and Measurements

The resonance behavior of the DUT was characterized using the custom-built setup described previously, with the displacement sensor omitted for this set of measurements. The DUT was connected via electrical feedthroughs to a vector network analyzer (VNA; FSH8, Rohde & Schwarz, Germany) located outside the main enclosure. This configuration enabled continuous monitoring of the reflection coefficient ($|S_{11}|$) during acoustic stimulation provided by a speaker.

Initially, a wideband S_{11} sweep was performed over a frequency range of 1−8 GHz to identify the device's resonance frequency, which appeared as a distinct dip in the S_{11} magnitude curve. A frequency marker was placed at the resonance dip—preferably on the steepest slope—to ensure sensitivity to small resonance shifts. The VNA was then operated in zero-span mode, in which frequency sweeping is disabled and the instrument continuously samples the signal magnitude at the selected frequency. This allowed for time-resolved monitoring of the magnitude of the reflection coefficient ($|S_{11}|$), effectively capturing dynamic variations in the DUT's resonance behavior.

The zero-span measurement settings were selected to accommodate a range of temporal resolutions. For example, a sweep time of 100 ms with 401 points yielded a sampling rate of approximately ∼6.5 kHz, while a 30-second sweep resulted in a sampling rate of ∼20 Hz. The resolution bandwidth (RBW) filter was adjusted to 3−4 kHz to ensure that sidebands due to amplitude modulation were not missed. Fourier transformation of the time-domain data enabled identification of modulation frequencies generated by the membrane's mechanical motion under acoustic stimulation, superimposed on the carrier signal.[51−53] Each measurement sequence was separated by a 2-second delay to allow system stabilization and automated data storage. All time-domain S_{11} traces were automatically saved directly to USB storage for further processing. The VNA was calibrated before each experiment to ensure measurement accuracy and repeatability throughout the characterization process.

Cough acoustic recording experiments described in Results and Discussion were conducted with voluntary participants who provided informed consent, in accordance with the principles of the Declaration of Helsinki (1964, revised in 2013), and with approval from the Human Research Ethics Committee (HREC) of Delft University of Technology. To evaluate the device under realistic operating conditions, a single human participant (male, healthy, 27 years old, BMI = 25.7) was recruited. The device was inserted into a biodegradable face mask (PLA mask, VIDA, USA) and connected to the VNA using the same measurement configuration. The participant was instructed to cough under controlled conditions in two separate experiments. In the first experiment, the VNA was set to zero-span mode with a 30-second sweep time and 4 kHz RBW to capture multiple cough events. The participant performed three coughs, spaced at 5-second intervals, allowing clear temporal separation of the acoustic signals. In the second experiment, the sweep time was reduced to 250 ms while maintaining the 4 kHz RBW, and the participant was instructed to produce three discrete coughs at different intensities—mild, moderate, and severe. The shorter sweep time increased the sampling frequency to approximately 3.1 kHz, which allowed the system to detect modulation frequencies of sound up to 500 Hz, in accordance with the Nyquist theorem. These variations were designed to assess the device's responsiveness to varying cough intensities. The relevant portions of the recorded S_{11} time-domain traces were extracted and further analyzed to characterize the dynamic response of the device to each cough profile.

Degradation Study of Device

A dedicated setup was prepared based on a previously established procedure.[54] A glass container was filled with 700 g of soil saturated with water and sealed airtight using a custom laser-cut PMMA (Plexiglas, The Netherlands) lid. The lid included feedthroughs for two inlet tubes (to allow water addition and gas release) and for inserting a humidity sensor probe (MP780117, Multicomp Pro, UK). Soil moisture was monitored and maintained above 90% throughout the test. The entire container was placed in an oven maintained at 70 °C to replicate industrial composting temperature conditions.

Strips of CA (25 μm), PLA (50 μm), and zinc (10 μm), as well as complete devices and face masks, were partially buried in the soil before sealing. At predefined intervals (10, 20, 30, and 40 days), the container was opened, and samples were retrieved, washed, dried, and weighed using an analytical balance (Resolution: 0.1 mg; XSR204, METTLER TOLEDO, Switzerland) to evaluate weight loss and physical degradation. After each measurement, the container was resealed and returned to the oven for continued incubation until the next time point.

Characterization of Device Performance under Varying RH and Flexing Conditions

A custom humidity chamber was constructed using a sealed polyethylene box to evaluate the performance of the device under controlled humidity conditions. Openings were drilled to allow insertion of a commercial temperature and humidity sensor probe (MP780117, Multicomp Pro, UK) for precise humidity calibration, as well as a power cable for the humidifier and a coaxial cable connecting the SMA port of the device inside the chamber to external measurement equipment. All other openings were carefully sealed with a silicone gun to maintain an airtight environment. An ultrasonic cool mist humidifier (H101, Homvana, China) was placed inside the chamber to regulate internal humidity levels. During testing, the humidifier was activated to gradually increase relative humidity (RH) to target levels of 40%, 65%, and 90%. Once each target RH was reached, the humidifier was turned off, followed by a 5-min stabilization period to ensure uniform environmental conditions before measurements.

To experimentally evaluate flexing conditions, the device was subjected to controlled mechanical bending cycles. PMMA circles with diameters ranging from 60 mm to 140 mm were cut using a laser cutter and used as bending supports. These circles were affixed to a Teflon base (5 cm height) to prevent the device from contacting the table surface during testing. The device was mounted onto the circular forms using heavy-duty double-sided tape (3M, USA), enabling repeatable bending at different radii to induce varying mechanical strain angles.

Throughout the humidity and flexing tests, the resonance behavior of the device was continuously monitored using the VNA connected via a coaxial cable to the SMA port of the device. Data acquisition and storage were performed using R&S Instrument View software, which provided remote control of the VNA and enabled data saving in various formats for subsequent analysis.

Data Processing and Statistical Analysis

Fast Fourier Transform (FFT) and Short-Time Fourier Transform (STFT) analyses were performed using OriginPro (OriginLab Corp., Northampton, USA). For FFT, the modulated time-domain signal was transformed into the frequency domain, with magnitudes expressed in decibels and normalized to a peak of 0 dB. The sampling rate was calculated from the time intervals in the signal. Short-Time Fourier Transform (STFT) analysis was carried out to evaluate the

https://doi.org/10.1021/acssensors.5c04572
ACS Sens. XXXX, XXX, XXX−XXX

time-dependent spectral content of the signal. The signal, originally recorded with a sampling frequency of 6200 Hz, was analyzed using a Hanning window of 256 samples to balance time and frequency resolution. A high overlap of 90% between adjacent windows was applied to ensure smooth temporal tracking of frequency components. The STFT was computed using a 4096-point FFT, providing fine frequency resolution. The frequency range was restricted to 0−1300 Hz to focus on relevant content. The final time-frequency map was visualized using a jet colormap and exported as a high-resolution image (600 dpi) for documentation and further analysis. For dielectric spectroscopy measurements, five points were measured on both the front and back surfaces of the films, and the standard deviation was calculated to assess measurement variability.

■ RESULTS AND DISCUSSION

Green Cough Sense enables contactless, real-time monitoring of respiratory disease progression by extracting acoustic signals from cough sounds. These acoustic parameters include fundamental frequency (associated with vocal fold vibration), sound intensity (related to acoustic pressure amplitude), and temporal patterning (e.g., duration and repetition rate).[4,5,24] At the core of the sensing system is a sound-sensitive, drum-like patterned periodic acoustic surface complex coupled with an underlying patch antenna. When exposed to cough-induced acoustic pressure waves, the surface undergoes mechanical vibrations that modulate the electromagnetic scattering parameters of the antenna through dynamic impedance mismatching induced by these vibrations. Figure 1a presents a schematic overview of the correlation between cough acoustics and lung health. In early-stage or mild infections, coughs typically exhibit low-frequency (<300 Hz), low-intensity, and irregular temporal profiles.[55−58] In contrast, advanced respiratory pathologies, such as tuberculosis, bronchitis, pneumonia, or COPD complications, generate high-frequency (300−600 Hz), high-intensity coughs with consistent temporal patterns.[3,4,59,60]

Figure 1b shows the system packaging, highlighting the integration of our fully biodegradable sensor into an off-the-shelf biodegradable face mask. The sensor is fabricated using a solvent-free, low-temperature green process, consisting of CO_2 laser-patterned layers of CA, PLA, and zinc, selected for their roles in acoustic sensitivity, mechanical support, and electrical conductivity, respectively. These layers are vertically stacked via thermal lamination, which represents the first demonstration of lamination in biodegradable device fabrication, offering a rapid, sustainable approach compatible with roll-to-roll manufacturing of flexible electronics. CA serves dual roles as both the structural substrate for the antenna and acoustic resonator, and as a thin vibrating membrane. As a derivative of cellulose, CA offers significantly enhanced thermoplastic processability while maintaining low electromagnetic loss, making it ideal for precise, solvent-free fabrication.[61,62] PLA provides mechanical integrity and acts as both a packaging layer and a spacer to minimize air damping beneath the membrane. Zinc functions as the conductive element for both the antenna patch and ground plane, selected for its relatively high electrical conductivity (1.69×10^7 S/m at room temperature) among biodegradable metals reported to date.[63] The device was integrated into a face mask with membranes facing the mouth and the antenna inside, enabling real-time cough detection while maintaining normal mask usage (Figure 1c). Figure 1d shows the partially degraded device and mask after one month of soil burial under industrial composting conditions (70 °C, 90−100% RH), confirming the composability of the system and its end-of-life sustainability.

Figure 1e illustrates the complete life cycle of Green Cough Sense from raw material selection to end-of-life reintegration into the environment. The cycle begins with the selection of biodegradable materials: CA from plant cellulose, PLA from corn starch, and zinc, a micronutrient metal, chosen for its sustainable origin and low environmental impact. The device is fabricated using cleanroom-free, green manufacturing methods, enabling energy-efficient, scalable production compatible with existing industrial infrastructure.[64,65] The system naturally degrades in compost or soil, breaking down into lactic acid, cellulose fragments, and zinc ions, which are non-toxic byproducts that support microbial activity and serve as nutrient-rich feedstock.[66−68]

Device Design, Fabrication, and Characterization

We developed a scalable, green process for fabricating biodegradable devices using laser machining and low-temperature lamination. This adhesive- and solvent-free method enables precise assembly of zinc, PLA, and CA layers into a compact antenna−resonator system (Figure 2). A CO_2 laser (λ = 10.6 μm) was used for high-precision, maskless patterning of zinc (10 μm), PLA (50 μm), and cellulose acetate (25−500 μm). Its strong photothermal interaction with metals and polymers enables localized ablation and clean edge definition, eliminating the need for chemical etching, photoresists, or cleanroom lithography. Precise fabrication of the conductive geometry of the antenna is accomplished using laser machining of the zinc layer (Figure 2a). The 10 μm-thick foil was patterned to form both the radiating patch (i.e., a rectangular patch with a microstrip feed line) and the ground plane, using 50 W power and 1 cm/s scan speed. Lower settings failed to achieve full cutting of the foil, while higher values led to thermal distortion and irregular, wavy edges, with dimensional tolerances deviating by up to 500 μm from the initial design. Next, a 50 μm-thick PLA film was used as a lamination pouch to encapsulate and mechanically stabilize the antenna structure (Figure 2b). PLA was chosen for its low dielectric loss ($\tan \delta \leq 0.05$) at microwave frequencies,[69] which supports a higher quality factor in antenna performance, and for its excellent thermoplastic processability, enabling low-temperature lamination without adhesives.[70] In addition, its high mechanical rigidity (Young's modulus ≈ 3.5 GPa), notable among polymeric biodegradable materials, provides the necessary structural support for stable device operation.[71]

CA was selected for its compatibility with laser micromachining, allowing precise patterning of all layers, and for its mechanical properties, including moderate stiffness (Young's modulus ≈ 1 GPa) and low density (1.3 g/cm^3), which enhance membrane displacement under acoustic pressure. Indeed, CA was laser-patterned into three distinct layers: antenna substrate, resonator base, and vibrating membrane (Figure 2c). Each thickness was optimized to balance functional performance and fabrication constraints: the 500 μm-thick substrate enabled a stable device substrate; the 100 μm resonator base provided mechanical stability while remaining within the 1 mm total interlayer gap allowed by the lamination rollers; and the 25 μm membrane was thin and flexible enough to vibrate in response to subtle acoustic pressure variations.

The layers were first manually stacked using alignment marks to ensure proper alignment, then placed between Teflon sheets to prevent sticking to the heated rollers during lamination. The

Figure 1. Green Cough Sense is an eco-friendly smart face mask that monitors respiratory health by analyzing cough acoustic signals: passive, battery-free, and entirely biodegradable, with zero electronic waste and manufactured using low-temperature, green processes. (a) The severity of respiratory complications can be assessed by analyzing cough sound dynamics, including intensity, duration, rate, and frequency components. (b) The system features a biodegradable polylactic acid (PLA) face mask housing a passive microphone, which integrates an array of drum-like membranes that vibrate in response to sound waves. These vibrations alter the near-field of an integrated patch antenna, modulating its electromagnetic scattering parameters. (c) Photographs of the wearable device, shown before and after partial degradation in soil. The microphone consists of a 3D vertical stack of laser-patterned layers made from cellulose acetate (CA), PLA, and zinc, bonded through a low-temperature lamination process. (d) Image of the partially degraded microphone and face mask after soil burial under industrial composting conditions. (e) Schematic of the device life cycle—from sourcing sustainable raw materials (including soil enriched by previously composted devices), through cleanroom-free green fabrication, to end-of-life biodegradation, returning safely to the environment as nutrient-rich soil. The male model imagery is partially AI-generated. In panel (e), the inset images of industrial composting, agricultural feedstock, and sustainable raw materials contain AI-generated elements.

https://doi.org/10.1021/acssensors.5c04572
ACS Sens. XXXX, XXX, XXX−XXX

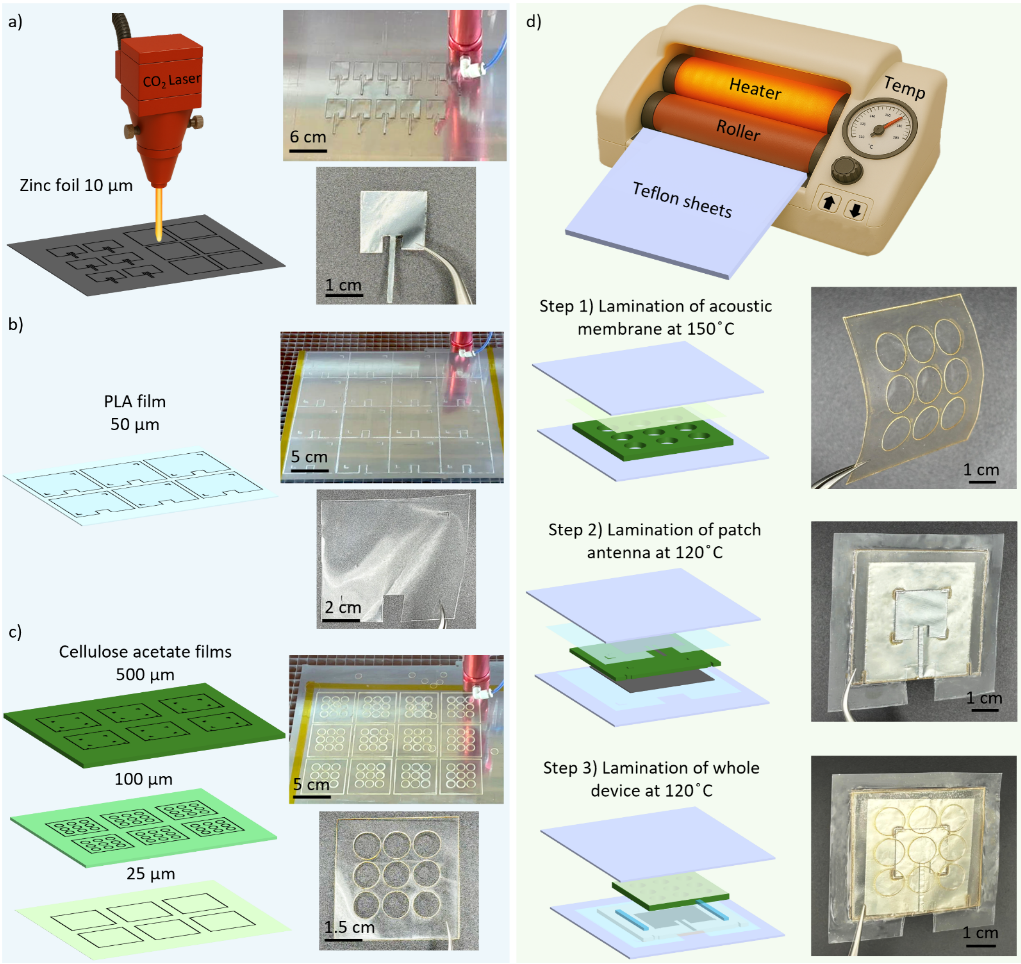

Figure 2. Green manufacturing of the biodegradable passive microphone. (a) Laser-patterned zinc foil defines the conductive element and ground layer of the patch antenna, which has a 2 × 2 cm patch and 2 × 19.5 mm microstrip feed section and a port section (not connected). (b) PLA is chosen for its low-loss dielectric properties in the microwave frequency range and its mechanical stability, making it suitable for encapsulating both the conductor and dielectric layers. (c) Cellulose acetate (CA) forms the antenna substrate, resonator substrate, and 3 × 3 array of drum-like acoustic resonators with 1 cm diameter and membrane due to its low acoustic loss and mechanical flexibility. (d) Lamination process stacks and bonds all functional layers at controlled temperatures, yielding the final, fully biodegradable device. The device sizes 6 × 6 cm, has a thickness of 0.8 mm, and weighs only 4 grams. In panel (a), the laser head image is partially AI-generated. In panel (d), the laminator schematic includes partially AI-generated elements.

stepwise thermal lamination process was tailored to the thermal and mechanical characteristics of PLA and CA (Figure 2d). Initially, the 25 µm CA acoustic membrane was bonded to the resonator base (CA; 100 µm) at 150 °C, which is below the glass transition temperature of CA, to promote controlled adhesion with minimal buckling. In the second step, the patch antenna layers (PLA, CA, and zinc) were laminated at 120 °C, well above the glass transition temperature of PLA (Tg = 50−65 °C), to ensure strong adhesion between the lamination pouches. Higher temperatures resulted in excessive deformation of the antenna structure post-lamination, adversely affecting its resonance performance. The acoustic resonator section was assembled onto the laminated antenna using 100 µm-thick spacer bars made of PLA, forming an air gap beneath each membrane to prevent contact with the antenna and reduce air damping. A step-by-step overview of the full device fabrication process, including laser cutting of the polymeric/metallic films, sequential lamination steps, and final assembly, is provided in the supplementary video (Movie S1).

Thickness measurements quantify lamination-induced thickness variability and confirm the dimensional stability of the PLA/PLA bilayer. Tensile testing to evaluate interfacial bonding showed that the PLA/PLA laminate exhibited the highest adhesion strength. Further details of the mentioned characterizations are provided in Note S1 and Figures S1 and S2, and the real-time tensile responses of all laminates are shown in Movie S2.

The antenna was fed via a microstrip transmission line, with feed geometry and substrate thickness tuned to achieve 50-ohm impedance matching, enabling accurate S-parameter measurements using a vector network analyzer (VNA). To do this, precise dielectric characterization is critical at the operating frequency (∼6 GHz), selected based on the required 6 × 6 cm^2 device size to fit within typical face mask dimensions. Accordingly, we analyzed the dielectric components over a broad frequency range (1−8 GHz) to extract their relative permittivity (ε_r) and loss tangent (tan δ), as shown in Figure 3a,b. Consistent with prior studies,[72,73] both materials exhibited a decreasing ε_r, from approximately 3.45 to 2.80 with increasing frequency, attributed to limited dipolar relaxation. In contrast, tan δ exhibited frequency-dependent fluctuations indicative of underlying dielectric relaxation phenomena. For CA, tan δ increased to a local maximum near ∼2.3 GHz, decreased toward 5 GHz, and rose again beyond 6 GHz. PLA showed a steep decline in tan δ from 1 to ∼3 GHz, followed by a plateau. These variations arise from the frequency-dependent reorientation of dipolar groups under an alternating electric field, with increased dielectric losses near characteristic relaxation frequencies. The trends are further influenced by polymer chain mobility and the degree of crystallinity within the material matrix.[74] Over the 1−8 GHz frequency range, the measured loss tangent values varied between 0.03 and 0.05 for CA, and 0 to 0.02 for PLA, corresponding to low-loss (tan δ ≤ 0.05) dielectric behavior.[75] Such characteristics are well-suited for achieving high-quality factors performance in biodegradable antennas. These measurements correspond to post-lamination films, as lamination (heat and pressure) can introduce interfacial air gaps or microbubbles that slightly alter the effective dielectric response, and measuring processed films eliminates this source of error.

All layers of the laminated structure were included in the model (Figure 3c), and a coaxial port was placed at the end of the microstrip feed line. Frequency-domain simulations yielded optimized dimensions for two device configurations. Devices 1 and 2 were designed with slight variations in patch length to examine their impact on resonance frequency and explore geometric tuning for operation across different frequency bands. For device 1 (red), the patch measured W: 20 mm, L: 19.5 mm, the microstrip feed line was W: 2 mm, L: 19.6 mm, and the ground plane was W: 40 mm, L: 45 mm. For device 2 (blue), the patch measured W: 20 mm, L: 20 mm, the microstrip feed line was W: 2 mm, L: 20.1 mm, with the same ground plane dimensions as device 1. The measured $|S_{11}|$ values were −18.3 dB at 6.40 GHz for device 1 and −17.13 dB at 6.27 GHz for device 2, both below −10 dB,[76] demonstrating predictable tuning behavior, as a ∼0.5 mm change in patch length produces a clear resonance shift. To minimize such variation, the CO_2 laser cutting parameters—laser power, repetition rate, and scan speed—were optimized for both polymer and metal layers to achieve the smallest stable kerf and avoid thermal overburn.[77] These conditions, summarized in Table S1, constrain the effective cut width to the 0.25 mm laser spot size and ensure reproducible patch dimensions with minimal tool-induced deviation.[78]

The simulated results (Figure 3d, dotted lines) closely matched the measured data. The shift in resonance aligns with standard patch antenna behavior, where shorter patch lengths yield higher resonance frequencies.[76] Accordingly, precise control of the patch length is essential to minimize error in the target resonance frequency. Figure 3e illustrates the measurement setup, where an SMA connector was mounted directly onto the feed line of the device, connecting the patch antenna to a VNA to sweep the reflection coefficient ($|S_{11}|$) over the frequency.[76] The simulated results (Figure 3d dotted lines) closely matched the measured data. The shift in resonance aligns with standard patch antenna behavior, where shorter patch lengths yield higher resonance frequencies.[76] The measured resonance at 6.40 GHz, with 3-dB points at f_L = 6.37 GHz and f_R = 6.43 GHz, corresponding to a 3-dB bandwidth of Δf_{3dB} = 60 MHz and a quality factor of $Q = f_0/\Delta f_{3dB}$ = 107 (Figure S3a and Note S1). The interrogation frequency is intentionally placed on the steepest portion of the resonance flank, where the $|S_{11}|$ is locally linear.[79] This ensures that small detuning effects produce proportional amplitude changes.[80] The linearity of this region and the corresponding regression analysis are provided in Note S2 and Figure S3.

The performance of the device under varying relative humidity (RH) is summarized by a 40 MHz resonance shift across

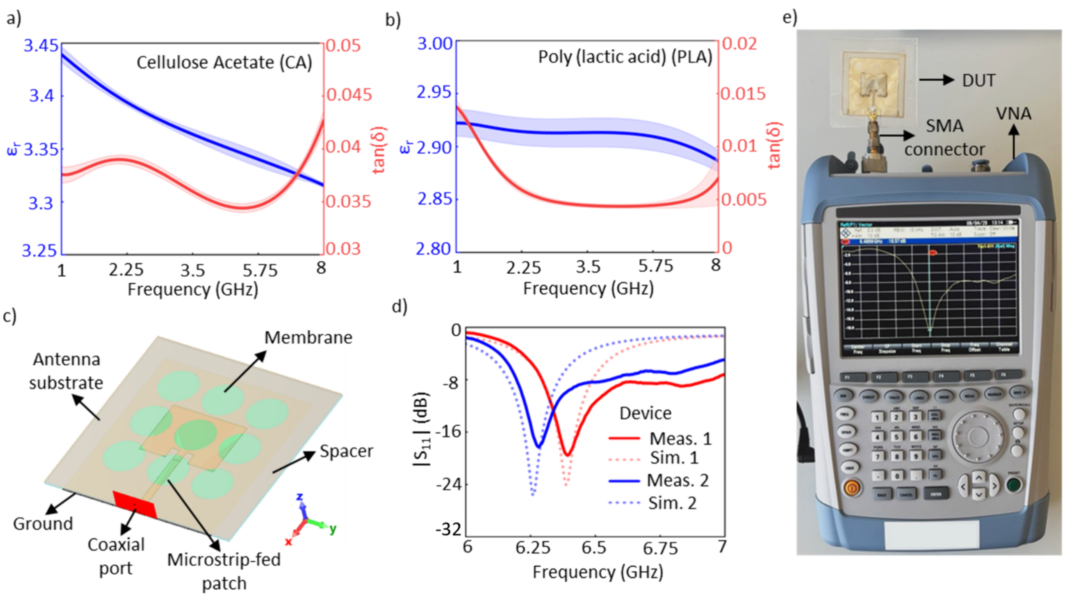

Figure 3. Dielectric characterization and resonance performance of the patch antenna. (a) Frequency-dependent relative permittivity (ε_r) and loss tangent (tan (δ)) of cellulose acetate. (b) Dielectric properties of poly(lactic acid) (PLA) measured from 1 to 8 GHz. Shaded regions indicate measurement error bars. (c) Electromagnetic model of the complete device in CST Microwave Studio used for simulations in this study. (d) Resonance behavior shown in simulated and measured input−port reflection coefficient ($|S_{11}|$) of devices with different patch lengths. (e) Measurement setup with the device under test (DUT) mounted via an SMA connector to a vector network analyzer (VNA) showing measurement of the reflection coefficient ($|S_{11}|$) across a 1 GHz frequency span.

https://doi.org/10.1021/acssensors.5c04572
ACS Sens. XXXX, XXX, XXX−XXX

40−90% RH. Additionally, bending introduces a linear frequency change over curvature radii from 60 to 140 mm (R^2 = 0.9979), as shown in Figures S4 and S5 and discussed in Notes S3 and S4 of the Supporting Information.

In short, the device employs a multilayer biodegradable architecture, integrating a passive patch antenna that simultaneously enables an interrogation interface in microwave range and a narrowband resonant acoustic sensor. The antenna's near-field response, within the sub-2 cm region dominated by non-radiative reactive fields, is modulated by a mechanically coupled membrane that vibrates in response to cough-induced acoustic pressure. Electromagnetic modeling in CST Microwave Studio was used to optimize the device dimensions for maximum impedance sensitivity to membrane displacement at the antenna's electrical resonance frequency. To evaluate acoustic performance, drum-shaped membranes were simulated in COMSOL Multiphysics using the frequency domain solver, focusing on displacement response within the cough sound frequency range. Maximizing sensitivity at these low frequencies required large diaphragm radii and thin membranes; therefore, CA films with a thickness of 25 μm, the thinnest commercially available sustainably sourced biodegradable film, were selected. The membrane diameter was maintained at 1 cm to match the optimized patch antenna size that enables array integration, which enhances near-field modulation coverage without increasing the device footprint.

Membrane Displacement Characterization under Monotone Acoustic Excitation

To characterize the out-of-plane displacement of the CA membrane, measurements were conducted using a custom setup (Figure 4a,b), as described in the Experimental Section. The sound pressure was calibrated to 90 dB SPL (0.6 Pa), and the membrane response was recorded under 400 Hz excitation.

Under 400 Hz excitation, the membrane exhibited a peak displacement of ∼17 μm (Figure 4c). Fast Fourier Transform (FFT) analysis (Figure 4d) confirms a dominant frequency at 400 Hz, while Short-Time Fourier Transform (STFT) results (Figure 4e) show consistent frequency content over time. Additional low-frequency spectral components observed at this drive frequency originate from nonlinear distortion in the loudspeaker when operated near its own acoustic resonance, which introduces extra frequency content into the excitation signal and is not related to membrane dynamics.[81−83]

Under 500 Hz excitation, the membrane was actuated in 3 distinct bursts, each reaching approximately 11 μm in displacement (Figure 4f). The corresponding FFT (Figure 4g) confirmed a dominant spectral peak at 500 Hz. The STFT (Figure 4h) shows sustained energy at 500 Hz, with weaker harmonics at 1 kHz and 1.5 kHz, indicating nonlinearity, as such overtones are absent in purely linear systems.[84] Similarly, under 600 Hz excitation, the membrane is actuated in 3 bursts, each reaching a peak displacement of approximately 8 μm (Figure 4i). The FFT (Figure 4j) confirms a dominant frequency component at 600 Hz. The STFT (Figure 4k) displays consistent spectral intensity at the fundamental frequency, along with weaker harmonics at 1.2 kHz and 1.8 kHz. These harmonic peaks originate from nonlinearities in the acoustic excitation, while the variation in displacement amplitude across frequencies reflects the viscoelastic and frequency-dependent mechanical response of the cellulose acetate membrane.[85−87] The maximum mechanoacoustic absolute sensitivity of the membrane, calculated as 0.045 μm/Hz, corresponds to the highest displacement response. These results indicate the membrane's suitability for acoustic sensing within the target cough frequency ranges.

Across all excitation conditions, a persistent ∼50 Hz peak is present in the FFT and STFT spectra. This peak is independent of the applied drive frequency and is therefore unrelated to membrane motion, originating instead from mains (AC) coupling within the excitation or sensing electronics.

To verify the experimentally observed membrane displacement at the center, a COMSOL Multiphysics frequency-domain simulation was performed on a drum-shaped single cellulose acetate membrane under a uniform 90 dB SPL (0.6 Pa) pressure load (Figure S6). The simulated displacement closely matches the experimental results and confirms the monotonic decline with increasing frequency, consistent with operation in the mass-controlled regime, where the amplitude decreases due to inertial and frequency-dependent damping effects. The simulation also shows negligible displacement below ∼150 Hz, confirming that the experimentally observed low-frequency peaks originate from the excitation system rather than membrane modes.[88,89]

In Vitro Assessment of the Green Cough Sense

Figure 5 presents a systematic investigation into the influence of membrane motion on the resonance behavior of a patch antenna under controlled acoustic excitation. Figure 5a illustrates the experimental characterization setup, which includes the circuitry used to generate and control the acoustic excitation signal delivered to the speaker, precisely regulating both the frequency and amplification level. This setup also integrates the VNA, which is connected to the DUT to monitor variations in the reflection coefficient ($|S_{11}|$). The configuration enables synchronized acoustic and RF measurement, ensuring accurate tracking of antenna response during membrane vibration. Figure 5b shows that the speaker, DUT, and reference microphone were each mounted on dedicated stands at calibrated distances to minimize parasitic effects such as acoustic reflections and electromagnetic interference. Single-tone excitations at 500, 550, and 600 Hz were applied through the speaker, and the resulting changes in $|S_{11}|$ were recorded using the VNA operating in zero-span mode.

To maintain consistent acoustic pressure across frequencies, the sound pressure level (SPL) was standardized to 90 dB SPL (re. 20 μPa), as demonstrated in Figure S7. The calibrated voltages applied to the amplifier circuit driving the speaker were 4.0 V for 500 Hz, 4.3 V for 550 Hz, and 4.8 V for 600 Hz, generating corresponding SPL values confirmed by the reference microphone. As a baseline, control measurements were performed with the speaker turned off to assess the system's response in the absence of acoustic excitation. The resulting $|S_{11}|$ signal (Figure S8a) reflected the noise floor of the readings, with FFT and STFT analyses (Figure S8b,c) confirming the lack of spectral or temporal features. The reference microphone data similarly showed no acoustic activity across time-domain, FFT, and STFT representations (Figure S8d−f).

Figure 5c shows the time-domain variation of the $|S_{11}|$ over 100 ms under 500 Hz acoustic excitation. A high sampling rate of 6.5 kHz was used to resolve the fundamental frequency and its harmonics. The periodic modulation in $|S_{11}|$, matching the 2 ms period of the 500 Hz sound wave, indicates that the membrane's vibration dynamically alters the antenna's

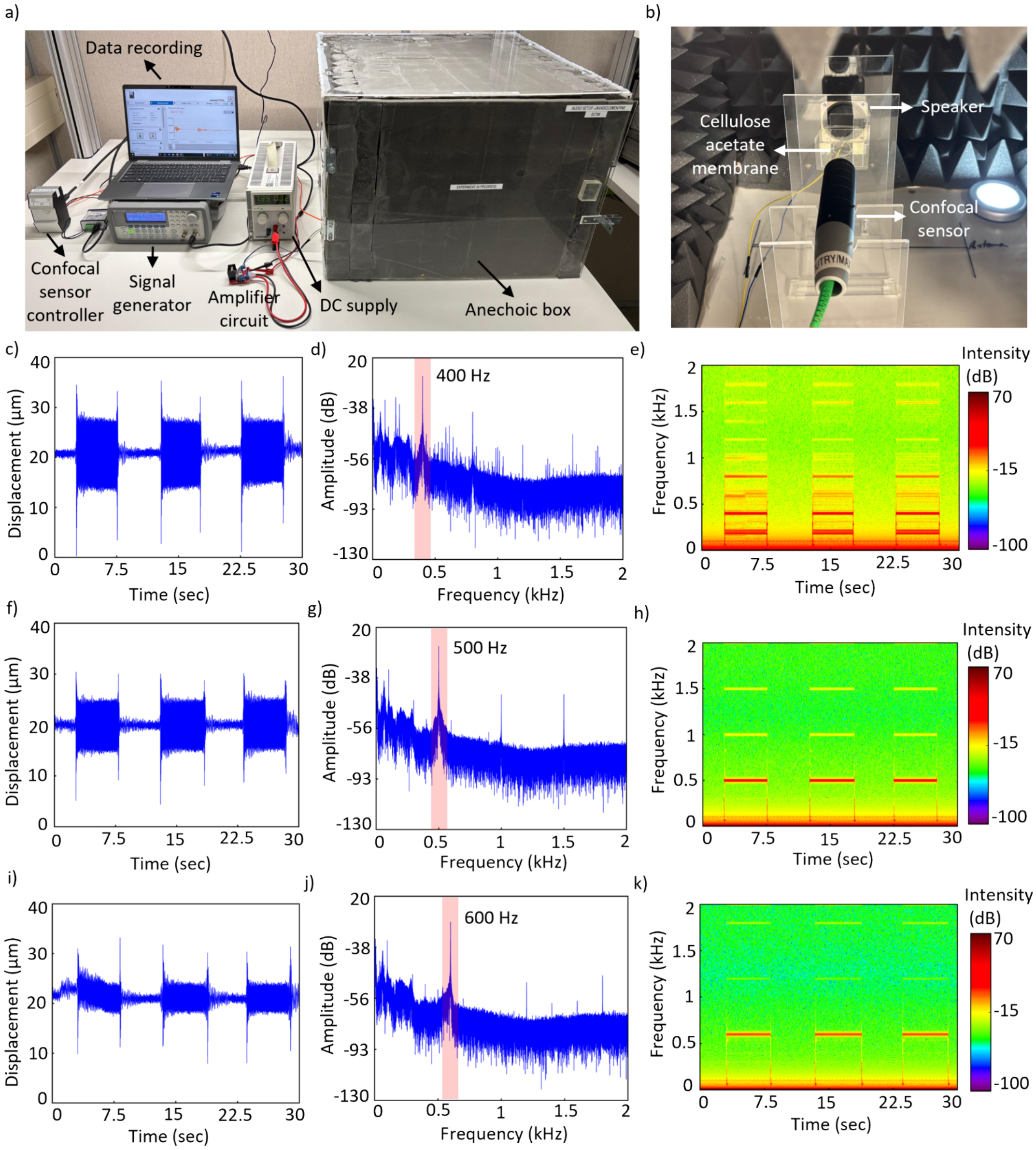

Figure 4. Membrane displacement characterization under varying acoustic excitations using a confocal laser displacement sensing system. (a) Custom-made experimental setup comprises an anechoic enclosure, a confocal displacement sensor, power amplifier circuitry, a signal generator, and the data acquisition system. (b) Interior view of the anechoic chamber showing the spatial arrangement of the cellulose acetate membrane, loudspeaker, and displacement sensor. (c) Time-domain membrane displacement measured via confocal sensing under 400 Hz acoustic excitation. (d) Frequency-domain analysis (FFT) of the 400 Hz signal, highlighting a dominant peak at the excitation frequency. (e) Short-time Fourier transform (STFT) depicting the temporal evolution and frequency characteristics of membrane vibration at 400 Hz. (f–h) Corresponding time-domain (f), FFT (g), and STFT (h) analyses of membrane displacement under 500 Hz acoustic excitation. (i–k) Time-domain (i), FFT (j), and STFT (k) representations of membrane displacement under 600 Hz acoustic excitation, illustrating fundamental frequency and harmonic components.

impedance. Figure 5d presents the FFT of $|S_{11}|$, exhibiting sidebands spaced at 500 Hz, indicative of amplitude modulation induced by acoustic excitation. The amplitude modulation depth is 0.08% of the carrier amplitude, corresponding to a sensitivity of 0.13%/Pa. Figure 5e displays the STFT of $|S_{11}|$, revealing persistent 500 Hz modulation and a second harmonic at 1 kHz, confirming stable and nonlinear acoustic-electromagnetic coupling in the DUT. This detuning disrupts the 50-Ω match and modulates the reflection coefficient, allowing the antenna to passively shift between reflective and absorptive states and thereby produce amplitude modulation suitable for backscatter-based wireless interrogation. The measured 0.08% change in $|S_{11}|$ sets the differential reflection coefficient that determines the strength of the wireless sidebands, and link-budget analysis indicates that this modulation depth provides sufficient received power and signal-to-noise ratio (SNR) for short-range microwave readout.[76,90] Based on this modulation depth and a representative backscatter link budget, the expected wireless operating distance is approximately 5−10 cm with compact reader antennas in necklace- or collar-mounted configurations.[91,92] The derivation of the effective modulated radar cross section and the corresponding interrogation range is provided in Note S5. On the readout side, a practical implementation uses a compact frequency-agile reader that performs a brief initialization sweep

https://doi.org/10.1021/acssensors.5c04572
ACS Sens. XXXX, XXX, XXX−XXX

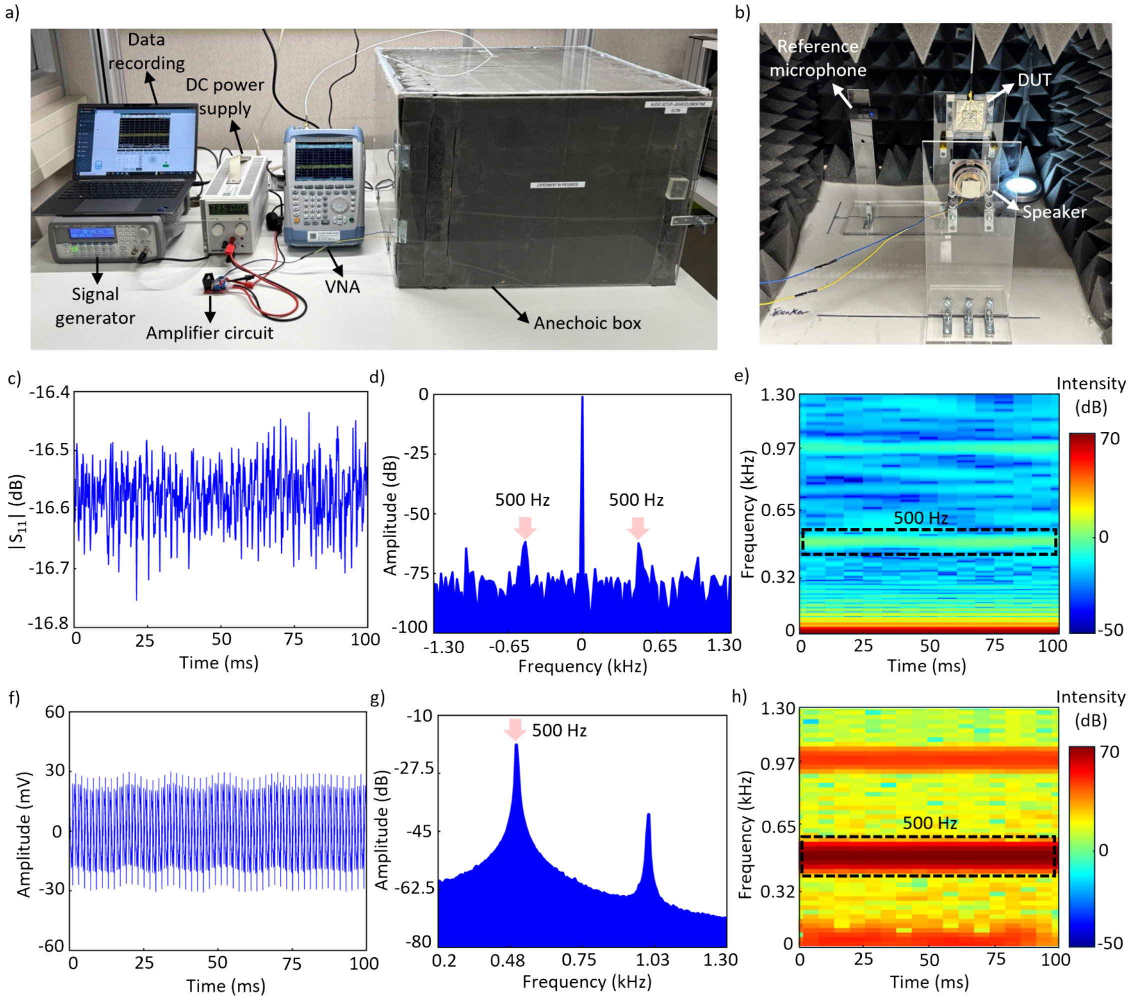

Figure 5. Characterization of the passive patch antenna-based device under single-tone acoustic excitation at 500 Hz. (a) Custom-made experimental setup. (b) Internal configuration of the anechoic chamber showing the device under test (DUT), reference microphone, and speaker placement. (c) Time-resolved measurement of the reflection coefficient magnitude of the DUT ($|S_{11}|$) captured by the VNA operating in zero-span mode with a built-in 4 kHz bandwidth filter. (d) FFT analysis of the $|S_{11}|$ reveals modulation frequencies around the carrier wave. (e) Short-time Fourier transform (STFT) of the $|S_{11}|$, highlighting a 500 Hz modulation frequency and its second harmonic. (f) Voltage signal recorded from the reference microphone simultaneously during the test. (g) Sound spectrum obtained via Audacity, displaying the fundamental acoustic tone at 500 Hz and its second harmonic, verifying the accuracy of the generated single tone. (h) STFT spectrogram of the reference microphone output, illustrating the persistence of the 500 Hz tone and its harmonic.

to locate the device-specific resonance, then locks the interrogation tone to the steep flank of the $|S_{11}|$ response to maximize sensitivity. After locking, the reader operates at a single fixed frequency and extracts the low-frequency amplitude modulation through a standard RF front end comprising a loop or patch antenna, a low-noise amplifier, and a detector or I/Q demodulator.[93−95]

Figure 5f−h validates the acoustic excitation conditions using the reference microphone. The time-domain signal in Figure 5f confirms the presence of a stable waveform, while the frequency-domain analysis in Figure 5g shows a strong 500 Hz peak with a minor second harmonic. The STFT in Figure 5h further confirms the continuous presence of the excitation. These results verify that the reference microphone accurately captured the 500 Hz sound from the speaker, ensuring the reliability of the acoustic input during the $|S_{11}|$ measurements.

Under acoustic excitation at 550 Hz and 600 Hz, the device exhibits $|S_{11}|$ modulation with clear spectral frequency components matching the applied tones (Figure S9 and Note S6). Sidebands observed in the FFT further confirm impedance modulation driven by the acoustic input. CST modeling of ±5 μm membrane displacement (Figure S10 and Note S7) shows a corresponding resonance shift, resulting in ∼2 dB of $|S_{11}|$ amplitude variation when monitored in zero-span mode, validating the mechanism underlying the measured acoustic modulation.

In Situ Assessment of the Green Cough Sense

To assess the performance of the Green Cough Sense system under practical conditions, it was evaluated using real coughs produced by a human subject (Figure 6a). The subject wore a face mask integrated with the biodegradable device, accompanied by a co-located commercial reference microphone used to record the acoustic signature of each cough. Figure 6b presents the real-time $|S_{11}|$ signal acquired in zero-span mode over the course of the coughing session. Nine distinct cough events

https://doi.org/10.1021/acssensors.5c04572
ACS Sens. XXXX, XXX, XXX−XXX

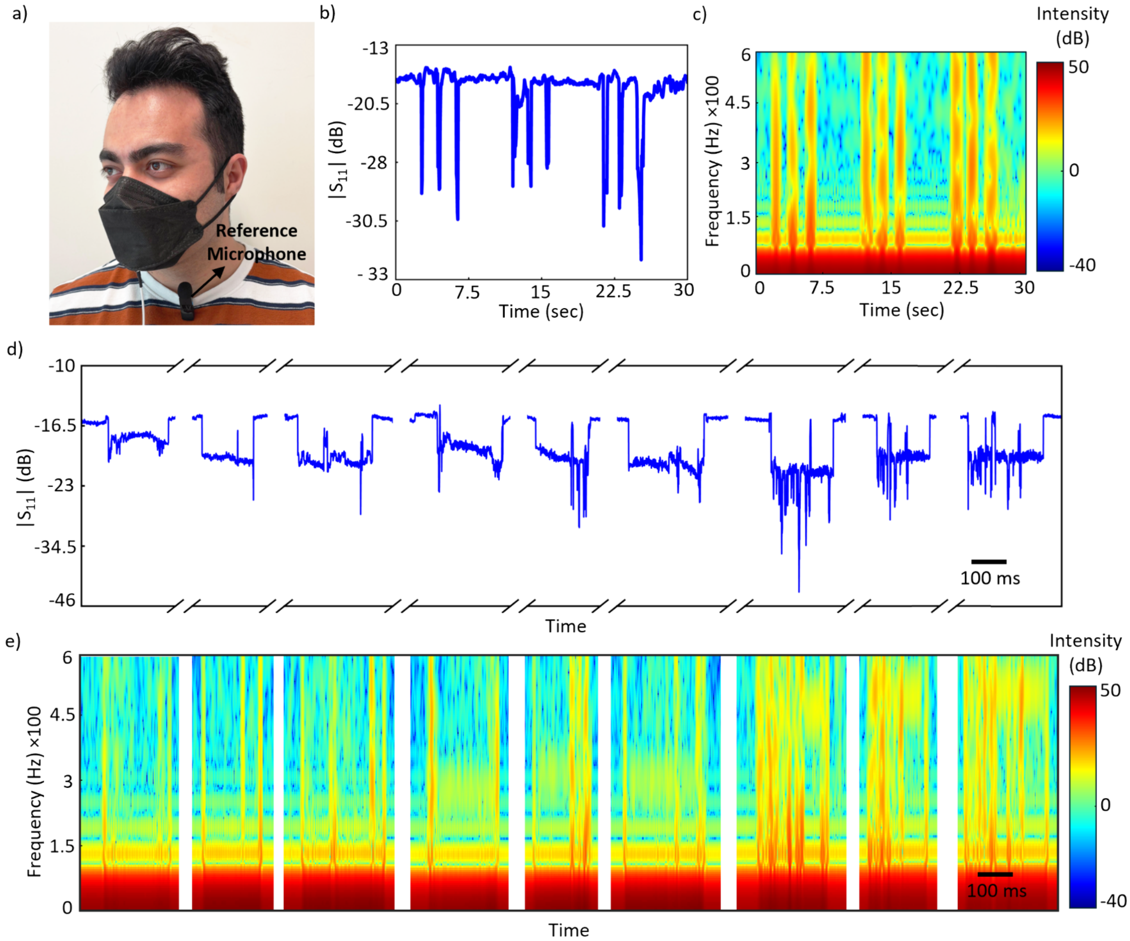

Figure 6. Evaluation of the green cough sense system for cough detection. (a) Photograph of a subject wearing the system and a co-located commercial active microphone serving as a reference benchmark. (b) Real-time measurement of the $|S_{11}|$ parameter in zero-span mode, capturing nine discrete cough events characterized by abrupt signal fluctuations. (c) Short-time Fourier transform (STFT) representation illustrating the spectral signatures of individual cough onsets over time. (d) Time-resolved $|S_{11}|$ trace showing dynamic responses to three distinct cough types: mild, moderate, and severe ($n = 3$ per each), recorded in zero-span mode. (e) STFT spectra corresponding to each cough type, revealing unique frequency patterns that differentiate cough severity levels.

are evident, each corresponding to abrupt amplitude changes, thereby demonstrating the sensitivity of the system to acoustically driven perturbations. The corresponding STFT plot in Figure 6c provides a time-frequency representation of the same data, clearly capturing the timing of each cough onset. However, due to the extended 30-second acquisition window in zero-span mode, the resulting low effective sampling rate (~50 Hz) limits the frequency resolution and precludes detailed spectral characterization of the cough sounds. A real-time recording capturing the temporal alignment of cough onsets is provided in Movie S3.

To enable finer temporal and spectral resolution in the analysis of cough severity, the time span of the zero-span mode on the VNA was reduced to 250 ms, thereby increasing the effective sampling frequency to approximately 2.6 kHz. This configuration enabled the reliable extraction of frequency components up to 500 Hz without aliasing, which was crucial for capturing the distinct spectral features of different cough types in subsequent measurements.

Figure 6d,e provides complementary insights into the ability of the system to distinguish between varying degrees of cough severity—mild, moderate, and severe—based on both time-domain and time-frequency responses. In Figure 6d, the time-resolved $|S_{11}|$ signals show clear, repeatable distinctions across the three cough categories. Mild coughs produce relatively small amplitude perturbations, reflecting limited membrane displacement and lower acoustic pressure. Moderate coughs result in more pronounced signal deviations with intermediate amplitude levels. In contrast, severe coughs yield the largest amplitude changes, accompanied by noticeable signal disruption, indicative of stronger acoustic impulses and greater membrane deflection. The recorded sound corresponding to each cough event is presented alongside the Figure 6d traces in the Supporting Information (Movie S4), enabling direct comparison between the acoustic input and the electromagnetic response of the system. Figure 6e highlights the distinct spectral profiles associated with each cough severity. Mild coughs exhibit low-frequency components primarily below 200 Hz, while moderate coughs show increased spectral energy centered around 300 Hz. Severe coughs display the broadest and most intense frequency content, extending up to approximately 600 Hz and including higher-pitched components. These results demonstrate that the microphone can successfully capture and differentiate cough events with varying severities, validating its potential for respiratory monitoring.

https://doi.org/10.1021/acssensors.5c04572
ACS Sens. XXXX, XXX, XXX−XXX

In a practical deployment, the passive device would not rely on zero-span measurements or short acquisition windows. Instead, it would be interrogated continuously by a dedicated RF reader transmitting a fixed continuous-wave carrier.[93,94] The reader's in-phase and quadrature (IQ) or envelope demodulation converts all membrane-induced amplitude and phase variations into baseband, where both the primary cough-induced modulation and its side peaks appear as distinct frequency components.[94] With standard low-pass filtering and anti-alias conditioning, an analog-to-digital converter (ADC) sampling at tens to hundreds of kilohertz can acquire the full modulation spectrum without aliasing, enabling accurate real-time reconstruction of cough signatures.[95] Using separate transmit and receive antennas, and optionally orthogonal polarization, minimizes self-interference and ensures sensitive detection of the weak acoustically modulated backscatter.[96,97] This architecture removes all sampling constraints associated with VNA zero-span mode, enabling robust real-time respiratory monitoring in practical settings.

Degradation of the "Green Cough Sense"

In line with the mission to achieve a zero-waste disposal at the end of life for single-use devices, complete environmental biodegradation is essential.[42,54,98] To this end, the industrial composting condition was simulated using a sealed chamber containing water-saturated compost soil, integrated with feedthroughs for water addition and gas extraction, and equipped with a moisture probe for precise soil moisture regulation (Figure 7a). Initial samples (Figure 7b) included the fully assembled device alongside strips of its constituent materials: zinc, PLA, and CA. PLA-based face mask and full device were partially embedded in soil to compare in-soil and above-soil degradation (Figure S11a,b). To quantitatively assess the degradation behavior, time-dependent weight loss was measured for both the full device and individual material strips. The results are presented in Figure 7c, showing a steady reduction in mass over 40 days under composting conditions. Biodegradation of the full device under simulated industrial composting conditions proceeded in a time-dependent manner. As shown in Figure 7d, after 10 days, the device exhibited visible signs of early degradation, including surface wrinkling, delamination, and color change in the PLA lamination pouch. This discoloration suggests thermal and hydrolytic stress affecting the PLA layer, which begins to degrade through hydrolysis of its ester bonds under high humidity and elevated temperature. Simultaneously, the CA layers within the device likely underwent initial hydrolytic deacetylation, making them more hydrophilic and vulnerable to further breakdown. By 20 days (Figure 7e), the PLA lamination layer had fully fragmented and delaminated from the device, indicating advanced hydrolytic degradation. The underlying cellulose acetate likely progressed from hydrolysis to microbial breakdown, while

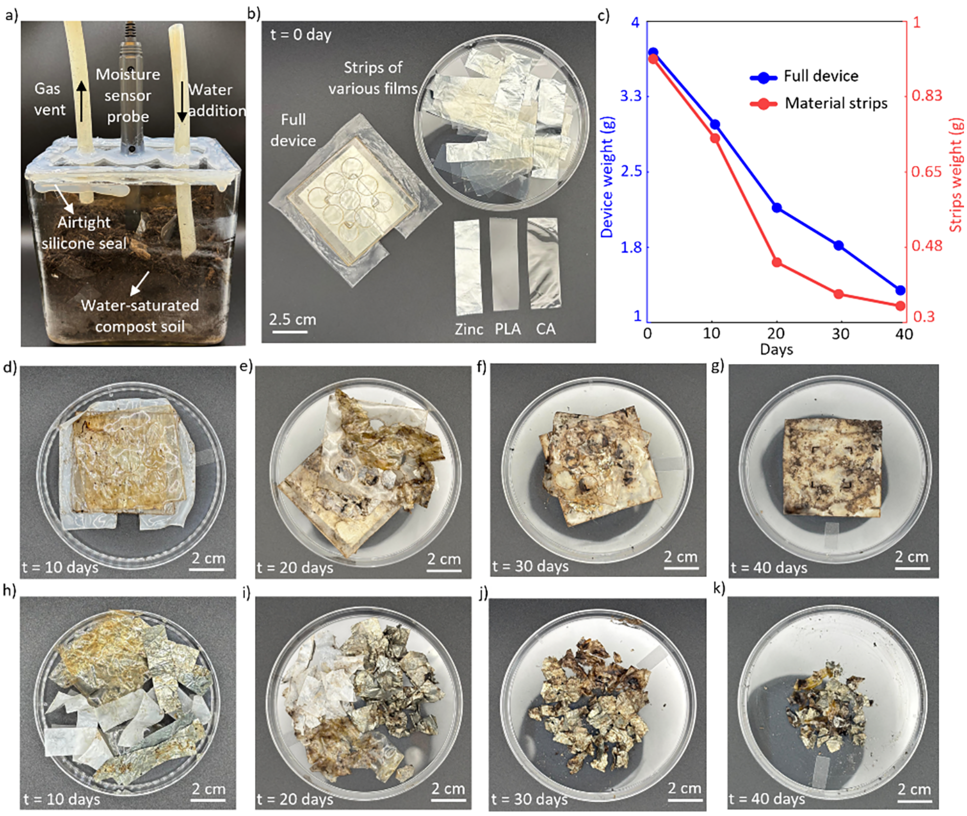

Figure 7. Simulated industrial composting conditions for the degradation of the device. (a) Custom-built setup mimicking industrial composting conditions. (b) Full device and strips of various films (zinc, PLA, and cellulose acetate) prior to degradation ($t = 0$ days). (c) Plot illustrating weight change over time for the full device (blue) and material strips (red), confirming gradual degradation under composting conditions (70 °C, >90% humidity). (d–g) Photographs of the full device after 10, 20, 30, and 40 days of composting, showing progressive physical degradation. (h–k) Photographs of individual material strips (zinc, PLA, and CA) after 10, 20, 30, and 40 days of composting, highlighting time-dependent degradation behavior.

https://doi.org/10.1021/acssensors.5c04572
ACS Sens. XXXX, XXX, XXX–XXX

structural failure was evident along the device edges. Similar hydrolysis and microbial-driven degradation behaviors in PLA and CA under composting or moist thermal conditions have also been reported in previous studies.[99−102] By 30 days (Figure 7f), the CA membrane was fully dissolved, cracks appeared in the CA resonator substrate, and the zinc layer was partially degraded. As shown in Figure 7g, after 40 days, the CA substrate of the acoustic resonator was degraded, and the total weight of the device decreased by 65%.

In parallel, the degradation of individual material strips, including zinc, PLA, and CA, was monitored under the same composting conditions. As shown in Figure 7h (10 days), zinc exhibited initial surface oxidation, PLA became opaque, and CA showed visible wrinkling, indicating early-stage hydrolysis. By 20 days (Figure 7i), degradation had advanced: zinc showed further oxidation and surface dulling, PLA became embrittled and partially fragmented, and CA exhibited increased brittleness and surface disruption, consistent with a transition from hydrolytic deacetylation to microbial degradation. These observations align with the weight loss trends in Figure 7c, confirming effective and time-dependent degradation of all constituent materials under simulated industrial composting conditions.[54] By 30 days (Figure 7j), the PLA strips were largely degraded in the soil, while the CA and zinc strips appeared more fragmented, indicating continued breakdown and material disintegration. By 40 days, as presented in Figure 7k, only small remnants of the CA and zinc components remained. These fragments exhibited markedly reduced volume and extreme mechanical fragility, such that even minimal physical force caused them to disintegrate into powder. This observation underscores the advanced stage of degradation for both materials. The mass of the full device decreased by 73% after 70 days (Figure S11c) and by over 90% after 100 days (Figure S11d), indicating almost full biodegradation and alignment with a zero-waste end-of-life cycle.

Table S2 (Supporting Information) compares our system with state-of-the-art mask-integrated audio sensors, emphasizing the distinctive advantages of our approach: a fully passive architecture, construction from entirely biodegradable materials, a sustainable fabrication process, and the capability for wireless readout without relying on non-biodegradable on-board batteries or electronics.

■ CONCLUSIONS

We report the simulation-assisted design, fabrication, characterization, and validation of Green Cough Sense—a biodegradable, battery-free, passive microphone-integrated smart face mask for unobtrusive, real-time cough monitoring and extraction of acoustic signals for pulmonary healthcare. Acoustic sensing is achieved via microwave interrogation of a membrane-integrated patch antenna whose reflection coefficient is mechanically modulated by sound-induced vibrations, eliminating the need for on-board batteries and non-biodegradable components that are prevalent in current mask-integrated monitoring systems. The device is fabricated entirely from sustainably sourced materials, including cellulose acetate (CA), poly(lactic acid) (PLA), and zinc, utilizing a solvent-free laser micromachining process and a low-temperature lamination technique. The mechanical stability of the laminated bilayers of CA and PLA was systematically investigated, confirming robust interfacial bonding essential for reliable device operation. Dielectric spectroscopy confirmed the low electromagnetic loss properties of the selected dielectrics within the operating frequency range (∼6 GHz), constrained by the size requirements for face mask integration; this low-loss behavior contributes directly to the high quality factor and narrowband performance of the patch antenna.

The multilayer structure is characterized using a vector network analyzer (VNA) connected via a coaxial cable, following standard practice for measuring the resonance frequency and reflection response of passive tags. Environmental humidity and bending induce predictable, quantifiable shifts in resonance frequency, indicating stable performance under realistic wearing conditions. Additionally, the effects of environmental humidity and device bending on the resonance frequency were examined, and the resulting shifts in resonance frequency were characterized, demonstrating the resilience and stable performance under realistic wearing conditions. Experimental investigations measured and confirmed the CA membrane displacement under acoustic excitation and demonstrated robust acoustic−electromagnetic coupling: the vibration of the laser-patterned drum-like membranes under cough sound modulates the reflection coefficient of the antenna, which was tracked in real time using the zero-span capability of a VNA. In this work, we also showed *in situ* validation of the system for detecting cough events and distinguishing between mild, moderate, and severe cough severities based on distinct acoustic frequency signatures. Furthermore, biodegradation studies conducted under simulated industrial composting conditions validated the 90% weight loss of the device after 100 days, ensuring a zero-waste end-of-life scenario.

For everyday use, the interrogation scheme still requires further development. Currently, readout relies on a wired benchtop VNA and therefore does not assess wireless performance or compact reader implementations. Future work should address this challenge.

■ ASSOCIATED CONTENT

Data Availability Statement

All the data gathered to reach the conclusions stated in this research were made available in the body of the text or the supporting information. However, if there are further requests, the authors will happily provide them upon request.

Supporting Information

The Supporting Information is available free of charge at https://pubs.acs.org/doi/10.1021/acssensors.5c04572.

Supplementary figures (S1−S11) include dimensional and mechanical characterization, device performance under varying acoustic, bending, and humidity conditions, degradation tests, and COMSOL and CST simulations; supplementary notes (Notes S1−S7) cover experimental details, materials and methods, calculation of quality factor, linear resonance bandwidth, and link budget model for wireless communication; supplementary tables (S1 and S2) summarize fabrication parameters and system comparisons (PDF)

Fabrication process (MP4)

Mechanical testing (MP4)

Green cough sense system in operation (MP4)

Varying cough intensities (MP4)

AUTHOR INFORMATION

Authors

Mohammad Javad Bathaei – *Department of Microelectronics, Delft University of Technology, Delft 2628 CD, The Netherlands*

Ata Golparvar – *Department of Microelectronics, Delft University of Technology, Delft 2628 CD, The Netherlands*

Sina Hashemi Zadeh – *Foundation for Research on Information Technologies in Society (IT'IS), Zurich 8004, Switzerland*

Denys Nikolayev – *Institut d'électronique et des technologies du numérique (IETR UMR 6164), French National Center for Scientific Research (CNRS)/University of Rennes, Rennes 35042, France*

Filipe Arroyo Cardoso – *Department of Microelectronics, Delft University of Technology, Delft 2628 CD, The Netherlands*

Clementine M. Boutry – *Department of Microelectronics, Delft University of Technology, Delft 2628 CD, The Netherlands*; orcid.org/0000-0002-6595-1478

Complete contact information is available at: https://pubs.acs.org/doi/10.1021/acssensors.5c04572

Funding

This research work is part of the 4TU-programme "Green Sensors". The "Green Sensors" is funded by the 4TU-programme High Tech for a Sustainable Future (HTSF). 4TU is the federation of the four technical universities in the Netherlands (Delft University of Technology, DUT; Eindhoven University of Technology, TU/e; University of Twente, UT; and Wageningen University and Research, WUR).

Notes

A patent application has been filed by M.J.B., D.N., and C.M.B. based on the work presented in this study.
The authors declare no competing financial interest.

ACKNOWLEDGMENTS

The authors would like to sincerely thank Mrs. Yaren Bathaei for her contributions to the degradation studies. Special thanks are also extended to Prof. Kasper Jansen from the Faculty of Industrial Design Engineering, TU Delft, as well as to technicians Ms. Mascha Slingerland for her assistance with the tensile test setup, Mr. Filip Simjanoski for his support with logistics, and Mr. Dennis van Bers for his support with the installation of the confocal sensor. M.J.B., F.A.C., and C.M.B. acknowledge support from the Dutch High Tech for a Sustainable Future (HTSF) 4TU Green Sensors grant. A.G. acknowledges the Swiss National Science Foundation (SNSF) fellowship.

REFERENCES

(1) Marchant, J. M.; Chang, A. B.; Kennedy, E.; King, D.; Perret, J. L.; Schultz, A.; Toombs, M. R.; Versteegh, L.; Dharmage, S. C.; Dingle, R.; Fitzerlakey, N.; George, J.; Holland, A.; Rigby, D.; Mann, J.; Mazzone, S.; O'Brien, M.; O'Grady, K. A.; Petsky, H. L.; Pham, J.; Smith, S. M. S.; Wurzel, D. F.; Vertigan, A. E.; Wark, P. Cough in Children and Adults: Diagnosis, Assessment and Management (CICADA). Summary of an Updated Position Statement on Chronic Cough in Australia. *Med. J. Aust.* **2024**, *220* (1), 35–45.

(2) Witjaksono, L. E.; Schulte, M.; Holland, A. E.; Wijsenbeek, M. S.; Khor, Y. H. Cough Monitoring Systems in Adults with Chronic Respiratory Diseases: A Systematic Review. *Eur. Respir. Rev.* **2025**, *34* (175), No. 230212.

(3) Ghrabli, S.; Elgendi, M.; Menon, C. Identifying Unique Spectral Fingerprints in Cough Sounds for Diagnosing Respiratory Ailments. *Sci. Rep.* **2024**, *14* (1), 1–8.

(4) Sharma, M.; Nduba, V.; Njagi, L. N.; Murithi, W.; Mwongera, Z.; Hawn, T. R.; Patel, S. N.; Horne, D. J. TBscreen: A Passive Cough Classifier for Tuberculosis Screening with a Controlled Dataset. *Sci. Adv.* **2024**, *10* (1), 1–14.

(5) Zimmer, A. J.; Ugarte-Gil, C.; Pathri, R.; Dewan, P.; Jaganath, D.; Cattamanchi, A.; Pai, M.; Grandjean Lapierre, S. Making Cough Count in Tuberculosis Care. *Commun. Med.* **2022**, *2* (1), 83.

(6) Serrurier, A.; Neuschaefer-Rube, C.; Röhrig, R. Past and Trends in Cough Sound Acquisition, Automatic Detection and Automatic Classification: A Comparative Review. *Sensors* **2022**, *22* (8), 2896.

(7) Sharan, R. V.; Rahimi-Ardabili, H. Detecting Acute Respiratory Diseases in the Pediatric Population Using Cough Sound Features and Machine Learning: A Systematic Review. *Int. J. Med. Inform.* **2023**, *176*, No. 105093.

(8) Dornelas, R.; Casmerides, M. C. B.; da Silva, R. C.; Victória dos Anjos Souza, M.; Pereira, L. T.; Ribeiro, V. V.; Behlau, M. Clinical Parameters of the Speech-Language Pathology Assessment of the Chronic Cough: A Scoping Review. *J. Voice* **2024**, *38* (3), 703–710.

(9) Chrysanthopoulou, A.; Kalogeropoulos, A.; Terzis, G.; Georgiopoulou, V.; Kyriopoulos, J.; Siablis, D.; Dimopoulos, J. Trends and Future Needs in Clinical Radiology: Insights from an Academic Medical Center. *Health Policy* **2007**, *80* (1), 194–201.

(10) Karuniawati, A.; Burhan, E.; Koendhori, E. B.; Sari, D.; Haryanto, B.; Nuryastuti, T.; Gayatri, A. A. A. Y.; Bahrun, U.; Kusumawati, R. L.; Sugiyono, R. I.; Susanto, N. H.; Diana, A.; Kosasih, H.; Naysilla, A. M.; Lokida, D.; Neal, A.; Siddiqui, S.; Lau, C. Y.; Karyana, M. Performance of Xpert MTB/RIF and Sputum Microscopy Compared to Sputum Culture for Diagnosis of Tuberculosis in Seven Hospitals in Indonesia. *Front. Med.* **2023**, *9* (January), 1–10.

(11) Stockl, K. M.; Tucker, J.; Beaubrun, A.; Certa, J. M.; Becker, L.; Chase, J. G. Real-World Use of Multiplex Point-of-Care Molecular Testing or Laboratory-Based Molecular Testing for Influenza-like Illness in a 2021 to 2022 US Outpatient Sample. *PLoS One* **2024**, *19* (11), 1–16.

(12) Tran, X. T.; Duong, K. L.; Bui, D. M.; Dang, K. L.; Hoang, N. T.; Bui, T. H.; Gautret, P.; Dao, T. L.; Hoang, V. T. High Prevalence and Risk Factors of Positive Sputum Smear in Newly Diagnosed Pulmonary Tuberculosis Patients in Vietnam. *Infez. Med.* **2025**, *33* (2), 212.

(13) Suo, J.; Liu, Y.; Wu, C.; Chen, M.; Huang, Q.; Liu, Y.; Yao, K.; Chen, Y.; Pan, Q.; Chang, X.; Leung, A. Y. L.; Chan, H-y.; Zhang, G.; Yang, Z.; Daoud, W.; Li, X.; Roy, V. A. L.; Shen, J.; Yu, X.; Wang, J.; Li, W. J. Wide-Bandwidth Nanocomposite-Sensor Integrated Smart Mask for Tracking Multiphase Respiratory Activities. *Adv. Sci.* **2022**, *9* (31), 2203565.

(14) Ye, Z.; Ling, Y.; Yang, M.; Xu, Y.; Zhu, L.; Yan, Z.; Chen, P. Y. A Breathable, Reusable, and Zero-Power Smart Face Mask for Wireless Cough and Mask-Wearing Monitoring. *ACS Nano* **2022**, *16* (4), 5874–5884.

(15) Ibrahim, W.; Natarajan, S.; Wilde, M.; Cordell, R.; Monks, P. S.; Greening, N.; Brightling, C. E.; Evans, R.; Siddiqui, S. A Systematic Review of the Diagnostic Accuracy of Volatile Organic Compounds in Airway Diseases and Their Relation to Markers of Type-2 Inflammation. *ERJ Open Res.* **2021**, *7* (3), No. 00030-2021.

(16) Ates, H. C.; Nguyen, P. Q.; Gonzalez-Macia, L.; Morales-Narváez, E.; Güder, F.; Collins, J. J.; Dincer, C. End-to-End Design of Wearable Sensors. *Nat. Rev. Mater.* **2022**, *7* (11), 887–907.

(17) Horváth, I.; Barnes, P. J.; Loukides, S.; Sterk, P. J.; Högman, M.; Olin, A. C.; Amann, A.; Antus, B.; Baraldi, E.; Bikov, A.; Boots, A. W.; Bos, L. D.; Brinkman, P.; Bucca, C.; Carpagnano, G. E.; Corradi, M.; Cristescu, S.; De Jongste, J. C.; Dinh-Xuan, A. T.; Dompeling, E.; Fens, N.; Fowler, S.; Hohlfeld, J. M.; Holz, O.; Jöbsis, Q.; Van De Kant, K.; Knobel, H. H.; Kostikas, K.; Lehtimäki, L.; Lundberg, J. O.;

Montuschi, P.; Van Muylem, A.; Pennazza, G.; Reinhold, P.; Ricciardolo, F. L. M.; Rosias, P.; Santonico, M.; van der Schee, M. P.; van Schooten, F. J.; Spanevello, A.; Tonia, T.; Vink, T. J. A European Respiratory Society Technical Standard: Exhaled Biomarkers in Lung Disease. *Eur. Respir. J.* **2017**, *49* (4), No. 1600965.

(18) Basanta, M.; Ibrahim, B.; Dockry, R.; Douce, D.; Morris, M.; Singh, D.; Woodcock, A.; Fowler, S. J. Exhaled Volatile Organic Compounds for Phenotyping Chronic Obstructive Pulmonary Disease: A Cross-Sectional Study. *Respir. Res.* **2012**, *13* (1), 72.

(19) Zhong, J.; Li, Z.; Takakuwa, M.; Inoue, D.; Hashizume, D.; Jiang, Z.; Shi, Y.; Ou, L.; Nayeem, M. O. G.; Umezu, S.; Fukuda, K.; Someya, T. Smart Face Mask Based on an Ultrathin Pressure Sensor for Wireless Monitoring of Breath Conditions. *Adv. Mater.* **2022**, *34* (6), 2107758.

(20) Knöpfel, G.; Baty, F.; Uhl, F.; Kern, L.; Brutsche, M. Quantification of Breathing Irregularity for the Diagnosis of Dysfunctional Breathing Using Proportional Tidal Sectional , Volume Variation : A Cross- - Retrospective Real- - World Study. *BMJ open* **2024**, *14*, No. e083401.

(21) Orlandic, L.; Dan, J.; Thevenot, J.; Teijeiro, T.; Sauty, A.; Atienza, D. October. How to count coughs: an event-based framework for evaluating automatic cough detection algorithm performance. In *2024 IEEE 20th International Conference on Body Sensor Networks (BSN)*; IEEE, **2024**, pp. 1–4.

(22) Alqudaihi, K. S.; Aslam, N.; Khan, I. U.; Shaikh, F. S.; Alsenbel, Y. M.; Alalharith, D. M. Cough Sound Detection and Diagnosis Using Artificial Intelligence Techniques: Challenges and Opportunities. *IEEE Access* **2021**, *9*, 102327–102344.

(23) Wieczorek, K.; Ananth, S.; Valazquez-pimentel, D.; Wieczorek, K. Acoustic Biomarkers in Asthma: A Systematic Review Acoustic Biomarkers in Asthma: A Systematic Review. *J. Asthma* **2024**, *61* (10), 1165–1180.

(24) Hegde, S.; Sreeram, S.; Alter, I. L.; Shor, C.; Valdez, T. A.; Meister, K. D.; Rameau, A. Cough Sounds in Screening and Diagnostics: A Scoping Review. *Laryngoscope* **2024**, *134* (3), 1023–1031.

(25) Benaliouche, H.; Hafi, H.; Bendjenna, H.; Alshaikh, Z. Towards AI-Driven Cough Sound Analysis for Respiratory Disease Diagnosis. *IEEE Access* **2025**, *13*, 92554–92568.

(26) Lentz-Nielsen, N.; Maaløe, L.; Madeleine, P.; Blomberg, S. N. Voice as a Health Indicator: The Use of Sound Analysis and AI for Monitoring Respiratory Function. *BioMedInformatics* **2025**, *5* (2), No. 31.

(27) Bertschinger, S.; Fenner, L.; Denecke, K. Feasibility of Cough Detection and Classification Using Artificial Intelligence in an Ambulatory Setting with a Ceiling Mounted Microphone. In *2023 IEEE 36th International Symposium on Computer-Based Medical Systems (CBMS)*; IEEE, **2023**, pp 660−665.

(28) Derrick, D.; Kabaliuk, N.; Longworth, L.; Pishyar-Dehkordi, P.; Jermy, M. Speech Air Flow with and without Face Masks. *Sci. Rep.* **2022**, *12* (1), 1–10.

(29) Groma, V.; Vörös, M.; Osán, J.; Madas, B. G.; Farkas, Á.; Kugler, S.; Müller, V.; Nagy, A. Characterization of Respiratory Particles Released during Continuous Speech and Its Relation to Mask Performance. *Sci. Rep.* **2025**, *15* (1), 1–12.

(30) Zhu, L.; Ha, T. D.; Chen, Y. H.; Huang, H.; Chen, P. Y. A Passive Smart Face Mask for Wireless Cough Monitoring: A Harmonic Detection Scheme With Clutter Rejection. *IEEE Trans. Biomed. Circuits Syst.* **2022**, *16* (1), 129–137.

(31) Wang, L.; Li, S.; Ahmad, I. M.; Zhang, G.; Sun, Y.; Wang, Y.; Sun, C.; Jiang, C.; Cui, P.; Li, D. Global Face Mask Pollution: Threats to the Environment and Wildlife, and Potential Solutions. *Sci. Total Environ.* **2023**, *887*, No. 164055.

(32) Baldé, C. P.; Kuehr, R.; Yamamoto, T.; McDonald, R.; D'Angelo, E.; Althaf, S.; Bel, G.; Deubzer, O.; Fernandez-Cubillo, E.; Gray, V.; Herat, S.; Honda, S.; Iattoni, G.; Khetriwal, D. S.; Luda di Cortemiglia, V.; Lobuntsova, Y.; Nnorom, I.; Pralat, N.; Wagner, M. *Global E-Waste Monitor 2024*; **2024**.

(33) Sutherland, L. J.; Vak, D.; Gao, M.; Peiris, T. A. N.; Jasieniak, J.; Simon, G. P.; Weerasinghe, H. Vacuum-Free and Solvent-Free Deposition of Electrodes for Roll-to-Roll Fabricated Perovskite Solar Cells. *Adv. Energy Mater.* **2022**, *12* (40), No. 2202142.

(34) Nath, D.; Misra, M.; Al-Daoud, F.; Mohanty, A. K. Studies on Poly(Butylene Succinate) and Poly(Butylene Succinate-Co-Adipate)-Based Biodegradable Plastics for Sustainable Flexible Packaging and Agricultural Applications: A Comprehensive Review. *RSC Sustainability* **2025**, *3*, 1267–1302.

(35) Khan, R.; Jolly, R.; Fatima, T.; Shakir, M. Extraction Processes for Deriving Cellulose: A Comprehensive Review on Green Approaches. *Polym. Adv. Technol.* **2022**, *33* (7), 2069–2090.

(36) Polylactic Acid Biopolymer Film. https://www.goodfellow.com/eu/polylactic-acid-biopolymer-film-1000225461.

(37) Cellulose Acetate Film. https://www.goodfellow.com/eu/cellulose-acetate-film-1000001893.

(38) Cho, Y.; Ninh, P. T. T.; Hwang, S.; Choe, S.; Myung, J. Sustainability Meets Functionality: Green Design Approaches to Cellulose-Based Materials. *ACS Mater. Lett.* **2025**, *7*, 1563–1592.

(39) Wang, Y.; Wang, K.; Chen, M.; Zhao, P.; Wang, Y.; Wang, X.; Han, X.; Wang, J. Development and Characterization of Biodegradable Bilayer Packaging Films Based on Corn Starch-Polylactic Acid as Raw Material. *J. Food Meas. Charact.* **2024**, *18* (1), 625–639.

(40) Najafi, M.; Forestier, E.; Safarpour, M.; Ceseracciu, L.; Zych, A.; Bagheri, A.; Bertolacci, L.; Athanassiou, A.; Bayer, I. Biodegradable Polylactic Acid Emulsion Ink Based on Carbon Nanotubes and Silver for Printed Pressure Sensors. *Sci. Rep.* **2024**, *14* (1), 1–15.

(41) Massonie, M.; Pinese, C.; Simon, M.; Bethry, A.; Nottelet, B.; Garric, X. Biodegradable Tyramine Functional Gelatin/6 Arms-PLA Inks Compatible with 3D Two Photon-Polymerization Printing and Meniscus Tissue Regeneration. *Biomacromolecules* **2024**, *25* (8), 5098–5109.

(42) Bathaei, M. J.; Singh, R.; Mirzajani, H.; Istif, E.; Akhtar, M. J.; Abbasiasl, T.; Beker, L. Photolithography-Based Microfabrication of Biodegradable Flexible and Stretchable Sensors. *Adv. Mater.* **2023**, *35* (6), 1–13.

(43) Yang, Q.; Liu, T. L.; Xue, Y.; Wang, H.; Xu, Y.; Emon, B.; Wu, M.; Rountree, C.; Wei, T.; Kandela, I.; Haney, C. R.; Brikha, A.; Stepien, I.; Hornick, J.; Sponenburg, R. A.; Cheng, C.; Ladehoff, L.; Chen, Y.; Hu, Z.; Wu, C.; Han, M.; Torkelson, J. M.; Kozorovitskiy, Y.; Saif, M. T. A.; Huang, Y.; Chang, J. K.; Rogers, J. A. Ecoresorbable and Bioresorbable Microelectromechanical Systems. *Nat. Electron.* **2022**, *5* (8), 526–538.

(44) Abbel, R.; Galagan, Y.; Groen, P. Roll-to-Roll Fabrication of Solution Processed Electronics. *Adv. Eng. Mater.* **2018**, *20* (8), 1–30.

(45) Kronenfeld, J. M.; Rother, L.; Saccone, M. A.; Dulay, M. T.; DeSimone, J. M. Roll-to-Roll, High-Resolution 3D Printing of Shape-Specific Particles. *Nature* **2024**, *627* (8003), 306–312.

(46) Bourely, J.; Kim, J.; Beyer, C.; Vorobyov, O.; Aeby, X.; Nyström, G.; Briand, D. Degradable and Printed Microstrip Line for Chipless Temperature and Humidity Sensing. *Adv. Electron. Mater.* **2024**, *10*, No. 2400229.

(47) Briand, D.; Molina-Lopez, F.; Quintero, A. V.; Ataman, C.; Courbat, J.; De Rooij, N. F. Why Going towards Plastic and Flexible Sensors?. *Procedia Eng.* **2011**, *25*, 8–15.

(48) Kania, H.; Saternus, M. Evaluation and Current State of Primary and Secondary Zinc Production—A Review. *Appl. Sci.* **2023**, *13* (3), 2003.

(49) Fallahi, A.; Hashemizadeh, S.; Kuster, N. On the Dielectric Measurement of Thin Layers Using Open-Ended Coaxial Probes. *IEEE Trans. Instrum. Meas.* **2021**, *70*, 1–8.

(50) Chen, J.; Liu, H.; Huang, Y.; Yin, Z. High-Rate Roll-to-Roll Stack and Lamination of Multilayer Structured Membrane Electrode Assembly. *J. Manuf. Processes* **2016**, *23*, 175–182.

(51) Chen, J.; Liu, H.; Huang, Y.; Yin, Z. High-rate roll-to-roll stack and lamination of multilayer structured membrane electrode assembly. *J. Manuf. Processes* **2016**, *23*, 175–182.

(52) Hemour, S.; Barbot, N.; Collin, F.; Lachaud, J.-L.; Destor, S.; Tomas, J. The Great Microwave Education Opportunity of the Great Seal Bug (Also Known as "The Thing"). In *54th European Microwave Conference*; **2024**.

https://doi.org/10.1021/acssensors.5c04572
ACS Sens. XXXX, XXX, XXX–XXX

(53) Faul, F. T.; Daubmeier, J.; Eibert, T. F. Measurement and Transformation of Continuously Modulated Fields Using a Short-Time Measurement Approach. *Adv. Radio Sci.* **2023**, *20*, 9–15.
(54) Rumley, E. H.; Preninger, D.; Shomron, A. S.; Rothemund, P.; Hartmann, F.; Baumgartner, M.; Kellaris, N.; Stojanovic, A.; Yoder, Z.; Karrer, B.; Keplinger, C.; Kaltenbrunner, M. Biodegradable Electrohydraulic Actuators for Sustainable Soft Robots. *Sci. Adv.* **2023**, *9* (12), No. eadf5551.
(55) Gupta, M.; Ahmed, S.; Kumar, R.; Altrjman, C. *Computational Intelligence in Healthcare: Applications, Challenges, and Management*; **2023**, CRC Press.
(56) Kuruma, K.; Otomo, T.; Sakama, T.; Akiyama, K.; Takakura, H.; Toyama, D.; Hirai, K.; Furuya, H.; Kato, M.; Mochizuki, H. Breath Sound Analyses of Infants with Respiratory Syncytial Virus Acute Bronchiolitis. *Pediatr. Pulmonol.* **2022**, *57* (10), 2320–2326.
(57) Salukhov, V. V.; Kharitonov, M. A.; Makarevich, A. M.; Bogomolov, A. B.; Kazantsev, V. A.; Ivanov, V. V.; Chugunov, A. A.; Morozov, M. A. Experience of Using the «Bark Vibrolung» Device in the Complex Treatment of Community-Acquired Pneumonia. *Vestn. Ross. Voen. Akad.* **2021**, *23* (1), 51–58.
(58) Battu, V. V.; Khiran Kumar, C. S.; Kalaiselvi Geetha, M. Lung Disease Classification Based on Lung Sounds—A Review. *Comput. Intell. Healthcare Informatics* **2024**, 233–250.
(59) Sarkar, M.; Madabhavi, I.; Niranjan, N.; Dogra, M. Auscultation of the Respiratory System. *Ann. Thorac. Med.* **2015**, *10* (3), 158–168.
(60) Htun, T. P.; Sun, Y.; Chua, H. L.; Pang, J. Clinical Features for Diagnosis of Pneumonia among Adults in Primary Care Setting: A Systematic and Meta-Review. *Sci. Rep.* **2019**, *9* (1), 1–10.
(61) Araújo, D.; Castro, M. C. R.; Figueiredo, A.; Vilarinho, M.; Machado, A. Green Synthesis of Cellulose Acetate from Corncob: Physicochemical Properties and Assessment of Environmental Impacts. *J. Clean. Prod.* **2020**, *260*, No. 120865.
(62) Chen, M.; Li, R. M.; Runge, T.; Feng, J.; Feng, J.; Hu, S.; Shi, Q. S. Solvent-Free Acetylation of Cellulose by 1-Ethyl-3-Methylimidazolium Acetate-Catalyzed Transesterification. *ACS Sustainable Chem. Eng.* **2019**, *7* (20), 16971–16978.
(63) Min, J. K.; Jung, Y.; Ahn, J.; Lee, J. G.; Lee, J.; Ko, S. H. Recent Advances in Biodegradable Green Electronic Materials and Sensor Applications. *Adv. Mater.* **2023**, *35* (52), 1–28.
(64) Punj, N.; Ahmi, A.; Tanwar, A.; Abdul Rahim, S. Mapping the Field of Green Manufacturing: A Bibliometric Review of the Literature and Research Frontiers. *J. Clean. Prod.* **2023**, *423*, 138729.
(65) Wang, Q.; Zhu, L.; Wang, M.; Cai, L.; Ye, H.; Zhang, Z.; Ren, Y.; Yang, Y.; Chen, C.; Ge, S.; Gan, W. Development of Eco-Friendly and Robust Structural Materials via Binder-Free Lamination of Waste Biomass with Help of Finite Element Method. *J. Clean. Prod.* **2024**, *449*, No. 141715.
(66) Natasha, N.; Shahid, M.; Bibi, I.; Iqbal, J.; Khalid, S.; Murtaza, B.; Bakhat, H. F.; Farooq, A. B. U.; Amjad, M.; Hammad, H. M.; Niazi, N. K.; Arshad, M. Zinc in Soil-Plant-Human System: A Data-Analysis Review. *Sci. Total Environ.* **2022**, *808*, No. 152024.
(67) Skrzypczak, D.; Izydorczyk, G.; Taf, R.; Moustakas, K.; Chojnacka, K. Cellulose-Based Fertilizers for Sustainable Agriculture: Effective Methods for Increasing Crop Yield and Soil Health. *Ind. Crops Prod.* **2023**, *205*, No. 117500.
(68) Gao, X.; Xie, D.; Yang, C. Effects of a PLA/PBAT Biodegradable Film Mulch as a Replacement of Polyethylene Film and Their Residues on Crop and Soil Environment. *Agric. Water Manage.* **2021**, *255*, No. 107053.
(69) Colella, R.; Chietera, F. P.; Michel, A.; Muntoni, G.; Casula, G. A.; Montisci, G.; Catarinucci, L. Electromagnetic Characterisation of Conductive 3D-Printable Filaments for Designing Fully 3D-Printed Antennas. *IET Microwaves Antennas Propag.* **2022**, *16* (11), 687–698.
(70) Surendren, A.; Mohanty, A. K.; Liu, Q.; Misra, M. A Review of Biodegradable Thermoplastic Starches, Their Blends and Composites: Recent Developments and Opportunities for Single-Use Plastic Packaging Alternatives. *Green Chem.* **2022**, *19* (11), 8606–8636.
(71) Wang, C.; Cai, L.; Gao, M.; Jin, L.; Sun, L.; Tang, X.; Shi, G.; Zheng, X.; Guo, C. Manufacturing of Membrane Acoustical Metamaterials for Low Frequency Noise Reduction and Control: A Review. *Mech. Adv. Mater. Struct.* **2023**, *31* (25), 7008–7023.
(72) Dichtl, C.; Sippel, P.; Krohns, S. Dielectric Properties of 3D Printed Polylactic Acid. *Adv. Mater. Sci. Eng.* **2017**, *2017* (1), 6913835.
(73) Khouaja, A.; Koubaa, A.; Ben Daly, H. Study of the Dielectric and Chemical Properties of Cellulose Bio-Based Composites. *Ind. Crops Prod.* **2024**, *214*, 118493.
(74) Lecoublet, M.; Ragoubi, M.; Leblanc, N.; Koubaa, A. Investigation of Thermomechanical and Dielectric Properties of PLA-CA 3D-Printed Biobased Materials. *J. Compos. Sci.* **2024**, *8* (6), 197.
(75) Mazierska, J.; Jacob, M. V; Ledenyov, D.; Krupk, J. Loss Tangent Measurements of Dielectric Substrates from 15K to 300K with Two Resonators: Investigation into Accuracy Issues. In *2005 Asia-Pacific Microwave Conference Proceedings*; IEEE, **2005**, Vol. 4, pp 4.
(76) Balanis, C. A. *Antenna Theory: Analysis and Design*; John wiley & sons, **2016**.
(77) Toren, P.; Smolka, M.; Haase, A.; Palfinger, U.; Nees, D.; Ruttloff, S.; Kuna, L.; Schaude, C.; Jauk, S.; Rumpler, M. High-Throughput Roll-to-Roll Production of Polymer Biochips for Multiplexed DNA Detection in Point-of-Care Diagnostics. *Lab Chip* **2020**, *20* (22), 4106–4117.
(78) Dreimol, C. H.; Guo, H.; Ritter, M.; Keplinger, T.; Ding, Y.; Günther, R.; Poloni, E.; Burgert, I.; Panzarasa, G. Sustainable Wood Electronics by Iron-Catalyzed Laser-Induced Graphitization for Large-Scale Applications. *Nat. Commun.* **2022**, *13* (1), 3680.
(79) Kananian, S.; Alexopoulos, G.; Poon, A. S. Y. Robust Wireless Interrogation of Fully-Passive RLC Sensors. *IEEE Trans. Circuits Syst. I Regul. Pap.* **2022**, *69* (4), 1427–1440.
(80) Abdolrazzaghi, M.; Genov, R.; Eleftheriades, G. V. A Single-Frequency Amplitude-Modulated RFID Portable Backscatter Surface Scanner for Near-Field Permittivity Imaging. *IEEE Access* **2025**, *13*, 201726–201740.
(81) Klippel, W. Tutorial: Loudspeaker Nonlinearities—Causes, Parameters, Symptoms. *J. Audio Eng. Soc.* **2006**, *54* (10), 907–939.
(82) Shushnov, M. S., Shushnova, T. V., Onoprienko, A. M. Non-Linear Acoustics In Loudspeaker Design. In *2025 IEEE XVII International Scientific and Technical Conference on Actual Problems of Electronic Instrument Engineering (APEIE)*; IEEE, **2025**; pp 1–6.
(83) Agerkvist, F. On the Impact of Loudspeaker Nonlinearities on Room Acoustic Measurements. In *DAS| DAGA 2025, 51st Annual Meeting on Acoustics*; Deutsche Gesellschaft für Akustik eV, **2025**.
(84) Temple, B.; Young, R. *The Nonlinear Theory of Sound*; **2023**, 1–76.
(85) Zhao, B.; Hu, J.; Chen, W.; Chen, J.; Jing, Z. A Nonlinear Uniaxial Stress-Strain Constitutive Model for Viscoelastic Membrane Materials. *Polym. Test.* **2020**, *90*, No. 106633.
(86) Dreux, X.; Majesté, J.-C.; Carrot, C.; Argoud, A.; Vergelati, C. Viscoelastic Behaviour of Cellulose Acetate/Triacetin Blends by Rheology in the Melt State. *Carbohydr. Polym.* **2019**, *222*, No. 114973.
(87) Appaw, C.; Gilbert, R. D.; Khan, S. A.; Kadla, J. F. Viscoelastic Behavior of Cellulose Acetate in a Mixed Solvent System. *Biomacromolecules* **2007**, *8* (5), 1541–1547.
(88) Hu, Y.; Zhang, J.; Long, J. Influence of Rubber's Viscoelasticity and Damping on Vertical Dynamic Stiffness of Air Spring. *Sci. Rep.* **2023**, *13* (1), 1–12.
(89) Wang, F.; Liao, J.; Huang, C.; Yu, H.; Yan, J.; Li, H. Study on the Damping Dynamics Characteristics of a Viscoelastic Damping Material. *Processes* **2022**, *10* (4), 1–15.
(90) Griffin, J. D.; Durgin, G. D. Complete Link Budgets for Backscatter-Radio and RFID Systems. *IEEE Antennas Propag. Mag.* **2009**, *51* (2), 11–25.
(91) Dang, N. H.; Tran, V. T.; Dang, T.-H.; Chung, W.-Y. Radio Frequency Energy Harvesting-Based Self-Powered Dairy Cow Behavior Classification System. *IEEE Sens. J.* **2023**, *23* (8), 8776–8788.
(92) Khan, S. R.; Bernassau, A. L.; Desmulliez, M. P. Y. Passive and Battery-Free RFID-Based Wireless Healthcare and Medical Devices: A Review. *IEEE J. Radio Freq. Identif.* **2024**, *8*, 724–742.

https://doi.org/10.1021/acssensors.5c04572
ACS Sens. XXXX, XXX, XXX–XXX

(93) Vigneau, F.; Fedele, F.; Chatterjee, A.; Reilly, D.; Kuemmeth, F.; Gonzalez-Zalba, M. F.; Laird, E.; Ares, N. Probing Quantum Devices with Radio-Frequency Reflectometry. *Appl. Phys. Rev.* **2023**, *10* (2), No. 021305.

(94) Laha, S.; Kaya, S. Radio Frequency IC Design with Nanoscale DG. *Analog Circuits*; **2013**, 19.

(95) Guo, X.; He, Y.; Nan, J.; Zhang, J.; Liu, Y.; Shangguan, L. A Low-Power Demodulator for LoRa Backscatter Systems with Frequency-Amplitude Transformation. *IEEE/ACM Trans. Netw.* **2024**, *32* (4), 3515–3527.

(96) Zargari, S.; Hakimi, A.; Rezaei, F.; Tellambura, C.; Maaref, A. Signal Detection in Ambient Backscatter Systems: Fundamentals, Methods, and Trends. *IEEE Access* **2023**, *11*, 140287–140324.

(97) Siddiqui, T. A. *Novel Modulated Backscattered Communication Techniques for Transponder Based on Multiple Antennas*. **2022**.

(98) Sethi, S. S.; Kovac, M.; Wiesemüller, F.; Miriyev, A.; Boutry, C. M. Biodegradable Sensors Are Ready to Transform Autonomous Ecological Monitoring. *Nat. Ecol. Evol.* **2022**, *6* (9), 1245–1247.

(99) Sedničková, M.; Pekařová, S.; Kucharczyk, P.; Bočkaj, J.; Janigová, I.; Kleinová, A.; Jochec-Mošková, D.; Omaníková, L.; Perďochová, D.; Koutný, M. Changes of Physical Properties of PLA-Based Blends during Early Stage of Biodegradation in Compost. *Int. J. Biol. Macromol.* **2018**, *113*, 434–442.

(100) Fogašová, M.; Figalla, S.; Danišová, L.; Medlenová, E.; Hlaváčiková, S.; Vanovčanová, Z.; Omaníková, L.; Baco, A.; Horváth, V.; Mikolajová, M.; Feranc, J.; Bočkaj, J.; Plavec, R.; Alexy, P.; Repiská, M.; Přikryl, R.; Kontárová, S.; Báreková, A.; Sláviková, M.; Koutný, M.; Fayyazbakhsh, A.; Kadlečková, M. PLA/PHB-Based Materials Fully Biodegradable under Both Industrial and Home-Composting Conditions. *Polymers* **2022**, *14* (19), 4113.

(101) Yadav, N.; Hakkarainen, M. Degradation of Cellulose Acetate in Simulated Aqueous Environments: One-Year Study. *Macromol. Mater. Eng.* **2022**, *307* (6), No. 2100951.

(102) Arrieta, M. P.; López, J.; Rayón, E.; Jiménez, A. Disintegrability under Composting Conditions of Plasticized PLA−PHB Blends. *Polym. Degrad. Stab.* **2014**, *108*, 307–318.

https://doi.org/10.1021/acssensors.5c04572
ACS Sens. XXXX, XXX, XXX−XXX